Doctoral Dissertations

Graduate School

5-2012

Laser-atom interactions: a multiresolution approach

Nicholas Eric Vence
nevence@utk.edu

To the Graduate Council:

I am submitting herewith a dissertation written by Nicholas Eric Vence entitled "Laser-atom interactions: a multiresolution approach." I have examined the final electronic copy of this dissertation for form and content and recommend that it be accepted in partial fulfillment of the requirements for the degree of Doctor of Philosophy, with a major in Physics.

<div align="right">Robert Harrison, Major Professor</div>

We have read this dissertation and recommend its acceptance:

Predrag Krstic, Joe Macek, Bob Compton, Thomas Papenbrock

<div align="right">Accepted for the Council:
<u>Dixie L. Thompson</u></div>

<div align="right">Vice Provost and Dean of the Graduate School</div>

(Original signatures are on file with official student records.)

Laser-atom interactions: a multiresolution approach

A Dissertation

Presented for the

Doctor of Philosophy

Degree

The University of Tennessee, Knoxville

Nicholas Vence

May 2012

This thesis is dedicated to the proposition that all men are created equal, that they are endowed by their Creator with certain inalienable Rights, that among these are life, liberty, and the pursuit of happiness.

Acknowledgements

I am grateful to the Department of Energy for funding and the National Center for Computational Sciences for computer time on what has intermittently been the world's fastest computer. My advisors have been the Yin and Yang of my graduate school existence. Predrag, you have been a fire of motivational in every sense of the word. I will remember the tireless hours you spent editing before deadlines going above and beyond the call of duty. Thank you. Thank you. Robert, I am in awe of your computational acumen. The level of Byzantine complexity through which you have fought to forge MADNESS is staggering. I remember walking into your office, for the first time; you gave me your undivided attention, answered my questions on Hund's rules, and kindled my curiosity in your research. I hope, someday, to inspire others as you have inspired me.

I have been blessed with solid teachers who have personally invested themselves in my life. Thank you for answering my questions and being examples at every step of the way. I thank physics faculty at Southern for setting me on trajectory. Dr. Caviness, you always took time to talk, even when you were swamped. I've relied on Mathematica countless times, and have come appreciate languages and literature. Dr. Kuhlman, I will never forget your unabashed eccentricities and deliberately difficult exams. Maybe some day I'll have my own mercy drawer. Dr. Hansen you created an optimal environment for learning E&M and quantum which me to the limit; I could not have learned more and it showed when I got to grad school. Dr. Hefferlin, I have had a roller coaster ride through physics over the past thirteen years. You

spent personal time with me on year one when I was crying my eyes out over calc apps, and you have kept in touch–which has been especially meaningful during the last two years of inexorably slow progress. Dad I would not be completing this PhD if it weren't for the rock solid foundation I received in algebra I and II; they allowed me to fall in love with physics.

In his book Outliers, Malcolm Gladwell stated that outstanding achievement has two requirements: dedication and a supportive community. I have had a great group of friends and coworkers. Deborah thanks for all the conversations you bring life and organization to our group. Scott and Jonny, we came in together and we're still trucking–it's been 7.5 years since our first year. I am fortunate to belong to a church which values higher education, and especially blessed to have Advent House in my life. It has been a good place to hang out, a nice spiritual community, and now a great place to live. Mom and Dad, you have valued education and providing me with the best you had. Mom, thanks to you I keep my kitchen spotless. You have always had time to listen to me, and it does my soul good to know that anytime I need to pour out my heart you are ready to listen. Dad your work ethic is unmatched, I'm glad some of it rubbed off. Your outspoken, gregarious nature has made me unabashed at speaking out or talking to speakers after meetings; not many people can say they have been snubbed by a Nobel laureate, but thanks to you I have that honer.

Finally, I want to thank The Divine for walking with me through this long and difficult road. I am privileged that you want to know my ups and downs. I have quoted James 1:5 scores of times asking for wisdom, and you have *never* let me down. I ask only that you help me reflect your character through both the lows and highs of life.

It is not the critic who counts; not the man who points out how the strong man stumbles, or where the doer of deeds could have done them better. The credit belongs to the man who is actually in the arena, whose face is marred by dust and sweat and blood, who strives valiantly; who errs and comes short again and again; because there is not effort without error and shortcomings; but who does actually strive to do the deed; who knows the great enthusiasm, the great devotion, who spends himself in a worthy cause, who at the best knows in the end the triumph of high achievement and who at the worst, if he fails, at least he fails while daring greatly. So that his place shall never be with those cold and timid souls who know neither glory of victory nor the agony of defeat.

—Teddy Roosevelt

Abstract

Isolated, attosecond laser pulses have allowed real-time measurement and control of electrons on atomic time scales. We present an explicit time-evolution scheme solving the time dependent Schrödinger equation, which employs an adaptive, discontinuous, spectral-element basis that automatically refines to accommodate the requested precision providing efficient computation across many length scales in multiple dimensions. This method is illustrated through time evolution studies of single electron atoms and molecular ions in three and four dimensions under the influence of intense, few-cycle laser pulses.

Contents

List of Tables

List of Figures

Chapter 1

Introduction

In the 1960s the invention of the laser revolutionized the study of Atomic, Molecular, and Optical (AMO) physics. The last decade has seen a similar avalanche of scientific breakthroughs as the generation and control of attosecond laser pulses have enabled a new wave of experiments: the time delay in electron tunneling [58, 14], the real-time observation of valence electron motion [22], tomographic imaging of molecular orbitals [28], and a wealth of new pump-probe experiments [29, 39, 27].

The development of *ab initio* computation in the AMO community has aided the explanation of various phenomena. For instance, in 1985 Chu and Cooper [12], aided by the personal computer revolution, published a non-perturbative solution to the Time-Dependent Schrödinger Equation (TDSE) that helped explain the frequency and intensity dependence of continuum-continuum transitions in laser-driven hydrogen. In the 1990s advances in synchrotron light sources led Pindzola and Robicheaux [49] to embrace parallel computing in their implementation of the two-electron TDSE for laser-driven He that enabled the study of correlated ionization processes. Sometimes new phenomena, like wave function vortices, are first discovered through *ab initio* calculations [44]. Other times experimental questions press for a computational explanation. Our story begins somewhere in the middle.

While studying carbon clusters ablated from the walls of a fusion reactor, Predrag Kristić did not find a satisfactory method for modeling the highly excited system. This intrigued Robert Harrison who was implementing a general-purpose, numerical scheme whose adaptive mesh offered an unbiased treatment of excitation and ionizations.

The realization of this multielectron scheme has, like most serious endeavors, experienced unexpected difficulties delaying the fulfillment. The prototype implementation, in python, time evolved a single electron and uncovered several design issues. Robert and his dedicated team of programmer-scientists have since forged an industrial-strength foundation optimized for parallel runtime upon which this version is constructed.

This dissertation probes the limits of treatment of single electron within the dipole approximation. It demonstrates convergence in the high-energy, multiphoton regime, and examines the exotic electron behavior in infrared, tunneling regime. Its generality is demonstrated by the extension of three dimensional (3D) atomic hydrogen to 3D molecular hydrogen ion, and finally, to a 4D molecular hydrogen ion by including the internuclear separation in the wave function. Two viable paths now exist: a 6D solution of the two-electron problem, and a multireference a multielectron system.

The remainder of the introduction reviews relevant physical processes and numerical methods. Chapter 2 explains the theoretical framework and key approximations of our solution to the TDSE. Chapter 3 introduces the multiresolution framework along with an implementation of our method. The convergence study (Chapter 4) and physical results (Chapter 5) of hydrogenic systems in an attosecond laser pulse are from my first paper [59]. The infrared pulse in Chapter 6 is the basis for my next publication. Chapter 7 compares the 3D and 4D representation of the the molecular hydrogen along with the effects of orientation.

1.1 Laser-atom fundamentals

Laser atom interactions have been studied since the inception of the laser in the early 1960s. Atoms in Intense Laser Fields [19] and Short Pulse Laser Interactions with Matter [20] provides the basis for much of this introduction.

1.1.1 Pondermotive effects

Freeman et al. [19] contributed a comprehensive introduction to the pondermotive potential. While it is not directly involved in few-cycle pulse domain, the pondermotive potential is of historical importance in characterizing a laser pulse.

Before Q-switching and mode-locking technologies [45], laser pulses were much longer. The carrier envelope phase was not necessary and the Fourier spectrum was close to a delta function. Electrons ionized by picosecond laser pulses often had an energy distribution characterizing the pulse rather than the atom. This masking of the physical processes was dubbed the pondermotive effect.

The average energy of an electron oscillating in a laser field is called the pondermotive energy

$$U_p = \frac{e^2 E_0^2}{4m\omega^2} \tag{1.1}$$

where e and m are the charge and mass of the electron and ω and E_0 are the frequency and intensity of the electric field. The pondermotive effect is seen for electrons ionized at the beginning and end of the pulse. When the change of pondermotive potential is on the same time scale as the exit time of the ionized electron, the photoionization energy is characterized by the laser

$$\delta E = \frac{\partial U_p}{\partial t} \delta t. \tag{1.2}$$

rather than the atomic ionization process. Long pulses where the majority of ionization occurs during a stable pondermotive energy are not influenced by this effect. Neither are few cycle pulses whose duration is much shorter than the exit

time of the photoelectron. While the pondermotive effect is largely forgotten, the pondermotive energy is still used to characterize laser pules.

1.1.2 Keldysh parameter

In 1964 Keldysh introduced a foundational view [30] of the behavior of single electron ionization in a laser field. That is, ionization is best described by tunneling or a multiphoton process based on the value of the Keldysh parameter

$$\gamma = \sqrt{\frac{I_p}{2U_p}} = \frac{\omega}{E}\sqrt{2I_p} \tag{1.3}$$

where U_p is the pondermotive energy from Eq. 1.1, I_p is the ionization potential, ω, and E are the laser's frequency, and electric field respectively. In the tunneling regime a strong, low-frequency field acts on a weakly bound electron. When $\gamma \ll 1$, ionization is best described by tunneling. In the multiphoton regime a weak, high frequency field ionizes a tightly bound electron. When $\gamma \gg 1$, ionization is best described by a few photons.

1.1.3 Multiphoton and above threshold ionization

Upon receiving enough energy, typically 5 - 25 eV in atoms, an electron will ionize. Since this corresponds to ultraviolet light, most optical materials, including air, react strongly with the beam; hence, the term vacuum ultraviolet (VUV). Thus, early experiments were performed with visible and infrared sources ($\omega < 3\,eV$). The available intensities were classified in the multiphoton regime (Fig. 1.2a) where the N-photon ionization rate

$$\Gamma_N = \sigma_N I^N \tag{1.4}$$

was well described by perturbation theory and strongly dependent on the laser intensity I.
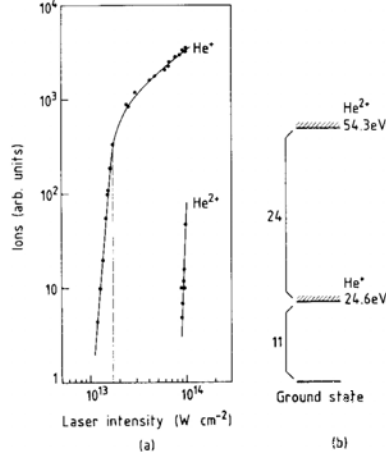
Figure 1.1: (from Lompré et al [36]) (a) A log-log plot of the variation in the number of He$^+$ and He^{2+} ions formed as a function of the laser intensity at 532 nm with a 40 ps laser pulse. (b) An energy level diagram of the 11- and 24-photon ionization of He and He$^+$.

Helium ($I_p = 24.6eV$) has the largest ionization potential of the atoms, making it a good case study for multiphoton ionization. Fig. 1.1 shows an experiment by Lompré et al. [36] where ion counts (He$^+$ and He^{2+}), presented as a function of laser intensity, are produced by (11-photon and 24-photon) ionization from a 40 ps laser pulse at 532 nm (2.3 eV). The vertical dotted line marks the onset of ground state depletion where the ionization rate deviates from that predicted by Eq. 1.4. The slopes of He$^+$ and He^{2+} (calculated from Fig. 1.1) confirm Eq. (1.4), and the onset of depletion marks the beginning of the non-perturbative regime.

As detectors improved and experiments moved away from simple ion counts towards electron detailed differential energy cross-sections. In 1979 Agostini and others noticed [2] peaks in the electron energy spectrum separated by units of the photon energy.

$$E = (N + S)\hbar\omega - I_p \tag{1.5}$$

This Above Threshold Ionization (ATI) occurs when the electron absorbs S photons beyond the N photons necessary for ionization. This is illustrated by Petite et al. [47] who studied xenon ($I_p = 12.1eV$) using a 135 ps pulse at 1064 nm with an
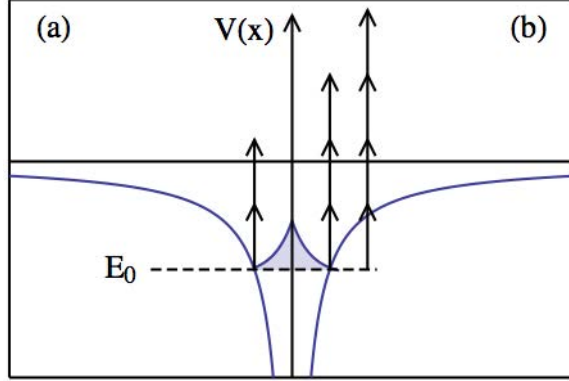
Figure 1.2: (a) An N-photon ionization where N is the minimum number needed rise above the threshold. (b) An $N + S$-photon ionization where $S = 1$ and 2.

intensity between $10^{12} - 10^{13} W/cm^2$. The photoelectron spectrum of xenon in Fig. 1.3 shows peaks separated by the photon energy (1.17eV). In the upper panel ($I = 2 \times 10^{12} W/cm^2$) the electron peaks decline with the number of photons as Eq. (1.4) and perturbation theory suggest. The lower panel peaks ($1 \times 10^{13} W/cm^2$) no longer follow the monotonic decline predicted by lowest order perturbation theory (LOPT). The electron-intensity dependence in the right panel shows a slope which only roughly corresponds to that of LOPT.

1.1.4 Over the barrier ionization

The advent of Chirped Pulse Amplification (CPA) in 1988 allowed the laser intensities to increase by several orders of magnitude. CPA involves stretching a pulse, amplifying the diluted signal, and recompressing it inside the interaction chamber. These intensities enabled the first experiments [4, 5] in the tunneling regime.

It is instructive to consider a classical model put forth by Bethe and Salpeter [8]. An electron bound to a Coulomb potential of nuclear charge Z in the presence of a laser (or uniform electric field) is constrained by a potential barrier

$$V(x) = \frac{-Z}{x} - \varepsilon x \tag{1.6}$$

6
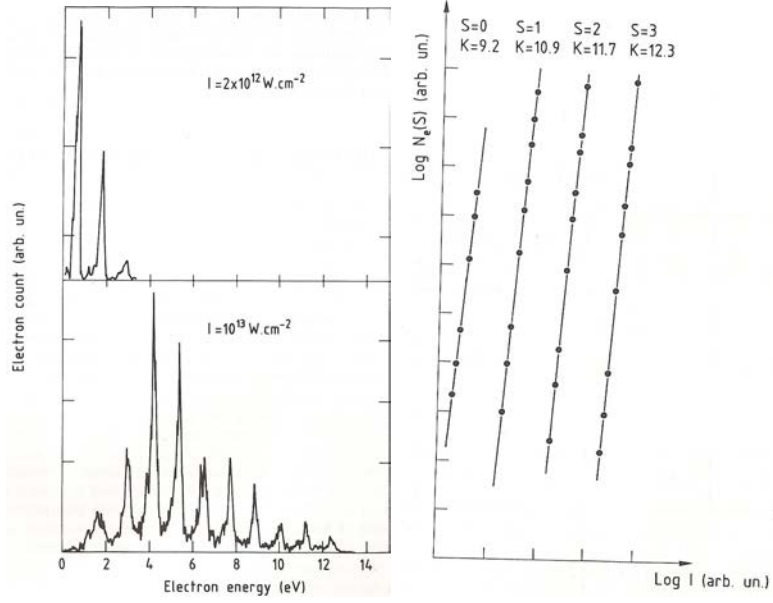
Figure 1.3: (from Petite et al. [47]) Two-electron energy spectra showing ATI of xenon at 1064 nm. (a) I $= 2 \times 10^{12} W/cm^2$ (b) I $= 1 \times 10^{13} W/cm^2$. (c) The log of the counts in each peak vs log of the intensity; the identical slope indicates the peaks correspond to the same order process.

that allows quantum mechanical tunneling (see Fig 1.4). For a sufficiently intense laser, the potential barrier will be lowered below that of the ground state. The critical electric field ε_c can be found by setting $\partial V(x)/\partial x = 0$, finding x_{max}, and setting $V(x_{max}) = E_0$ which yields

$$\varepsilon_c = \frac{E_0^2}{4Z} \tag{1.7}$$

$$I_{app} = \frac{c}{8\pi}\varepsilon_c^2 \simeq 4 \times 10^9 \left(\frac{I_p}{eV}\right)^4 Z^{-2} \ W/cm^2. \tag{1.8}$$

I_{app} is experimentally defined [4] as the lowest intensity producing 10 counts. This Over The Barrier Ionization (OTBI) brings nearly complete ionization as the intense laser field wrests the electron from the parent atom.
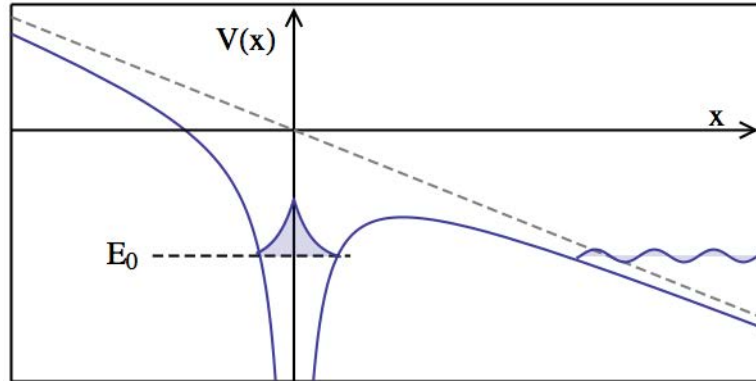
Figure 1.4: The laser field superimposed on the Coulomb potential. The electron in the ground state can now tunnel through the finite barrier; should the field be strong enough the atom will spontaneously ionize as the electron spills over the barrier.

Table 1.1: The critical intensity inducing over the barrier ionization.

	E_i $[eV]$	I_{app} $[W/cm^2]$
H (1s)	13.6	1.4×10^{14}
He$^+$ (1s)	54.4	8.8×10^{15}
Li^{2+} (2s)	30.6	3.9×10^{14}

1.1.5 High harmonic generation

In 1987 Shore and Knight [56] predicted that high energy photons would be the result of a highly ionized electrons recombining with the parent ion. McPherson et. al. [40] produced the predicted High Harmonic Generation (HHG) later that year. The photo-emission spectra of HHG is similar to the electron ionization spectra of ATI with peaks being separated by even integer multiples of the photon energy. First, the electron tunnels out of the atom (Fig. 1.5a) appearing above the threshold
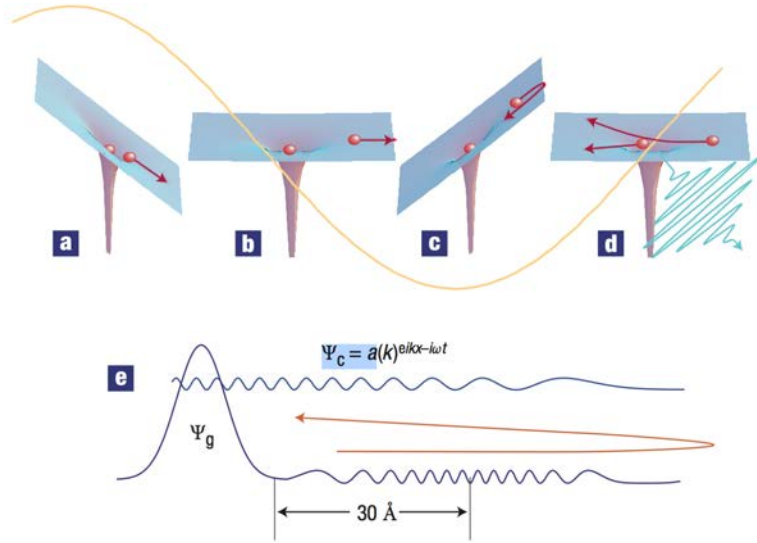
Figure 1.5: (from Corkum and Krausz [13]) The non-linear process of High Harmonic Generation (a) the electron tunnels through the energy barrier in the strong laser field appearing in the continuum initially at rest. (b) the electron is accelerated far from the atom (c) the oscillating field causes the electron to return to the nucleus where it (d) can be reabsorbed generating a high-energy photon. (e) A quantum mechanical representation of recombination.

with no initial velocity. Next, the electron is carried far from the atom absorbing many photons (Fig. 1.5b). As the oscillating field changes direction (Fig. 1.5c), the electron is accelerated towards the nucleus where there is a finite probability of recombination with the parent atom (Fig. 1.5d). Finally, the energy gained from the field is deposited in a single high energy photon.
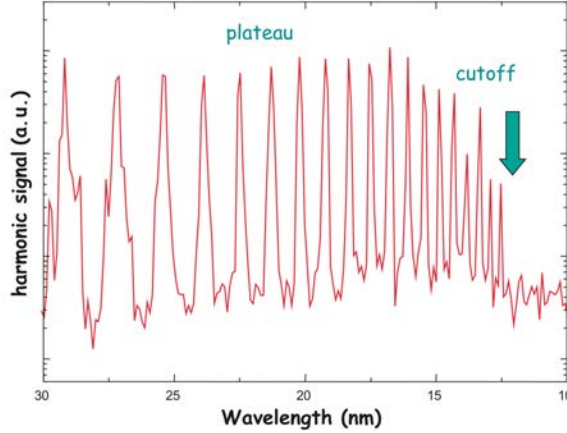
Figure 1.6: (from Agostini and DiMauro [1]) A partial high harmonic spectrum of neon irradiated by an 800nm, 50 fs pulse. The corresponding energy spectrum has equidistant peaks separated by 3.1 eV–twice the photon energy of the Ti:Sapphire laser. Two characteristics of HHG, the plateau and cutoff, are clearly shown.

In 1992, Krause et al.[31] predicted the maximum energy

$$E_{max} = I_p + 3.17U_p \tag{1.9}$$

of the photonionization spectrum (see Fig. 1.6) for an electron bound by an ionization potential I_p and driven by a field with pondermotive energy U_p. While, this analysis explains the highest harmonic expected for a given laser pulse, it does not explain the intensities of the harmonic spectrum. These were accounted for in 1994 when Lewenstein et al. [35] developed a full semi-classical theory explaining HHG in terms of the path-integral approximation of the TDSE.

1.2   Attosecond physics

In their well-illustrated review, Ferenc Krausz and Misha Ivanov [32] discuss the historical and technological foundation of the lightwave revolution which has driven the Atomic Molecular and Optical (AMO) community during the past decade. The figures and ideas in this sections come from this review.

1.2.1 History

Before 1900, Toepler used time separated electric sparks to generate and photograph sound waves. By varying the time interval he captured their motion creating the first pump-probe experiment. The development of the laser around 1960, marked by a discontinuity of slope in Fig. 1.7, precipitated a rapid increase in time resolution. The invention of the transistor in the 1970s allowed high speed electrical switching
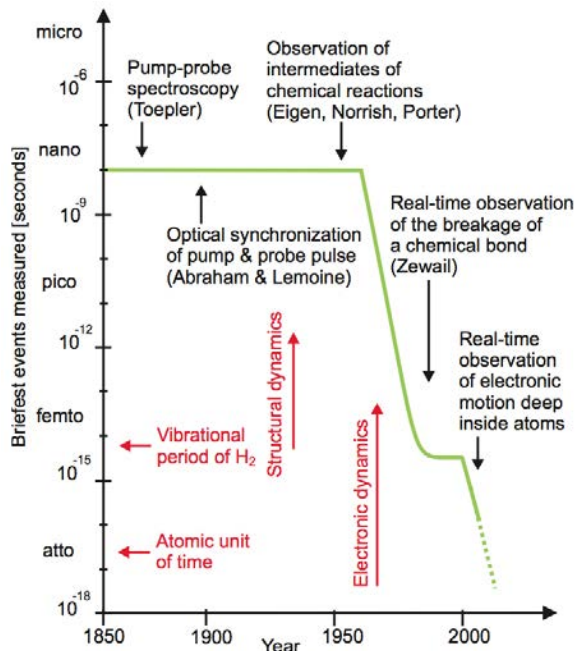
Figure 1.7: (from Krause and Ivanov [32]) The frontier of time resolution for realtime observation of microscopic processes. Discontinuities represent revolutions in technology.

moving the frontier of time resolution from the nanosecond to the picosecond domain and enabling the study of lattice vibration in solids and large molecules (see Fig. 1.8). These lattice vibrations, however, lead to a resolution-limiting dispersion. Optical materials with a stable refractive index allowed the creation of intense laser pulses in the 1980s approaching one femtosecond. These pulses allowed realtime measurements of rotation and vibration of the smallest molecules; however, the advance in resolution plateaued in the 1990s as the pulse duration reached the oscillation period of light. The 2000s have witnessed the stabilization and control of the Carrier Envelope

Phase (CEP) (see 1.2.2) in these few-cycle pulses allowing the production of isolated, attosecond pulses. Pulses at this resolution currently probe valence electron dynamics [18], and recent advances in laser technology [51] will extend the scope of this probe to core electrons.
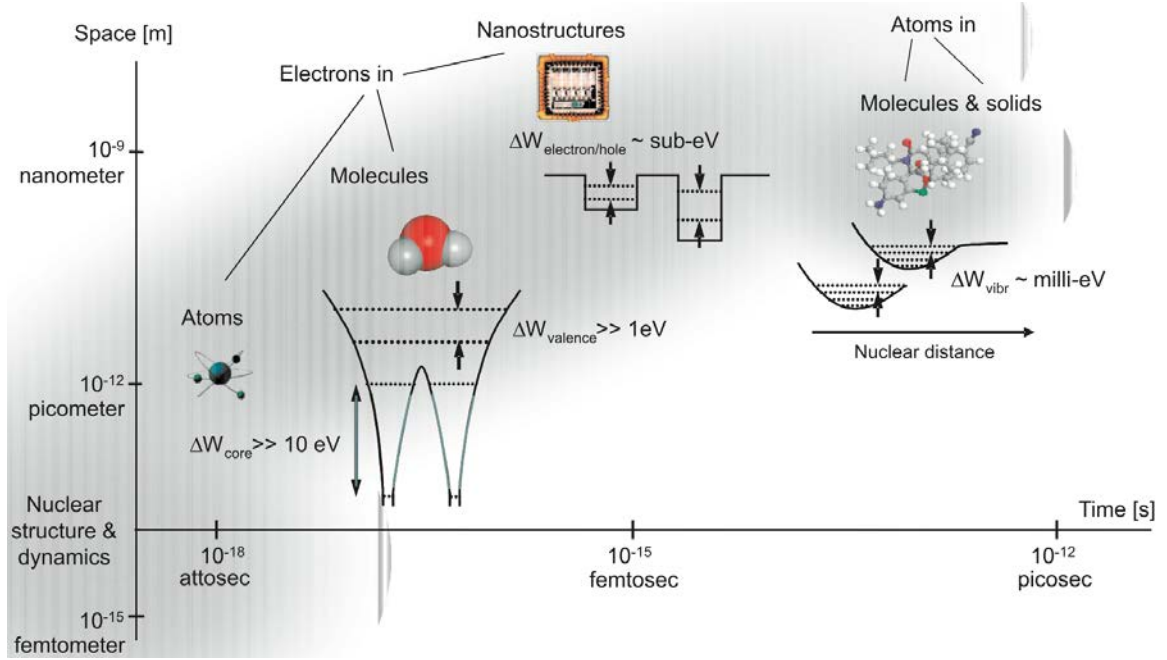
Figure 1.8: (from Krause and Ivanov [32]) Characteristic length and time scales in matter.

1.2.2 Carrier envelope phase

Long electron pulses are completely characterized by the driving frequency, pulse length, and intensity. Complete description of few-cycle pulses

$$
\mathbf{E}(t) = \cos(\omega t + \varphi) \begin{cases} \sin\left(\frac{\omega t}{2n_{cy}}\right) \\ \exp\left(-4\ln_2\left(\frac{\omega t}{2\pi n_{cy}}\right)^2\right) \end{cases} \tag{1.10}
$$

usually defined by a $\sin^2$ or Gaussian envelope require a phase φ to characterize the maximum of the envelope and driving frequency ω. Fig. 1.9 shows how this Carrier

Envelope Phase (CEP) φ substantially alters a two-cycle pulse. Its stabilization and control is responsible for the attosecond laser pulses / lightwave electronics revolution.
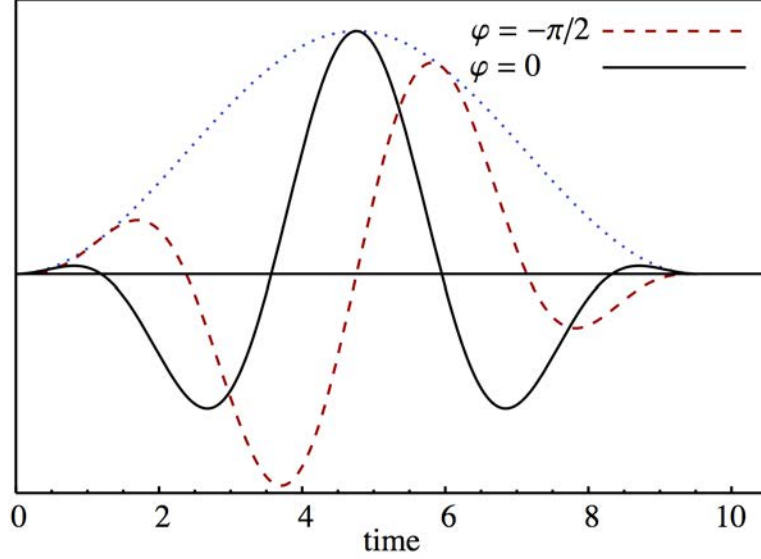
Figure 1.9: Pulses $\mathbf{E}(t) = \sin^2(\omega t/4)\cos(\omega t + \varphi)$ with different carrier envelope phases φ.

1.3 Computational techniques

The photoionization of atomic hydrogen may be the most studied problem in physics. Bethe and Salpeter [8] published a closed form expression for pre-laser, low-intensity, one-photon radiation. In the multiphoton regime, high frequencies and low intensities, multiphoton ionization is well accounted for by Perturbation Theory (PT). According to PT the photoionization probability

$$P_{ion}^{(n)} = \sigma_n I^n \tau \tag{1.11}$$

where $\sigma_{(n)}$ is the n photon cross section, I is the laser intensity (assumed constant), and τ the exposure time. Perturbation theory assumes a gentle pulse envelope and a weak intensity laser. The focused laser intensity increased in the late 1980s with

13

the advent of chirped pulse amplification and again in the 1990s with broadband titanium sapphire crystals These technologies led to peak intensities on the order of $10^{20}W/cm^2$ [43] –well above the failure point of PT which has been witnessed at intensities above $I \simeq 5 \times 10^{12}W/cm^2$ [15] (see Fig. 1.3). While PT has adequately described some non-linear processes like ATI [48] and even attosecond pulse dynamics [52], it is generally distrusted without comparison to more fundamental methods.

A variety of *ab initio* solutions to the TDSE fill the void of PT presenting an array of strengths and deficiencies. This survey of computational techniques will provide perspective as we introduce another solution to the TDSE.

1.3.1 Non-interacting particles

A general *ab initio* simulation for an N_e electron system requires $3N_e$ dimensional spatial grid which is numerically impractical for more than two electrons. The Single Active Electron (SAE) approximation has been a valuable tool in describing the classical behavior of strongly driven electrons in the tunneling regime. Its simplicity and speed make it a first choice even for multielectron systems as Scrinzi et al. [55] demonstrated by successfully comparing static ionization rates from the SAE approximation to those from integration of the full two electron TDSE. It breaks down in polyatomic molecules having excited bound states within a few eV of the initial state [38].

S-Matrix

In their comprehensive review of the intense many-body S-matrix theory [6] Becker and Faisal refer to an article on ATI [7] for a direct introduction to this multifaceted method. The application of S-matrix theory to intense atomic processes in the tunneling regime may be thought of as advanced perturbation theory.

The large excursion amplitude of an electron driven by a field in the tunneling regime is the basis of the primary simplification of the Hamiltonian,

$$H(t) = -\frac{\hbar^2}{2m}\nabla^2 + H_I(t) \tag{1.12}$$

that is, the selective choice of the interaction Hamiltonian H_I. This simplification allows the use of a compact, analytic basis throughout the problem. When the field is off, the electron feels that atomic potential $H_I = -Z/r$ of nuclear charge Z, and the Coulomb functions are used. When the field is on, $H_I = \mathbf{r} \cdot \mathbf{E}(t)$, and the Volkov functions

$$\psi_{\mathbf{p}}^V = | \mathbf{p} - e\mathbf{A}(t)\rangle e^{-iS_{\mathbf{p}}(t)} \tag{1.13}$$

are used. $| \mathbf{p} - e\mathbf{A}(t)\rangle$ is a plane-wave state $\langle \mathbf{r} | \mathbf{p} - e\mathbf{A}(t)\rangle = (2\pi)^{-3/2} e^{i[\mathbf{p}-e\mathbf{A}(t)]^2 \cdot \mathbf{r}}$ and

$$S_{\mathbf{p}}(t) = \int^t dt' \big[\mathbf{p} - e\mathbf{A}(t)\big]^2. \tag{1.14}$$

The description of the electron is obtained by the correlation amplitude.

$$M_{\mathbf{p}} = -i \int_{-\infty}^{\infty} dt_0 \, \langle \psi_{\mathbf{p}}^V(t_0) \mid H_I(t_0) \mid \psi_0(t_0)\rangle \tag{1.15}$$

The saddle-point approximation is often used in the multiphoton regime ($\gamma < 1$) where a weakly bound electron is driven by an intense, low-energy field. This approximation involves expanding the phase of the integrand about its stationary points. For an initial state $| \psi_0(t)\rangle = \exp(iE_{IP}t) | \psi_0\rangle$ this involves determining the solution of

$$\frac{d}{dt}\big[E_{IP} + S_{\mathbf{p}}\big] = E_{IP} + \tfrac{1}{2}\big[\mathbf{p} - e\mathbf{A}(t)\big]^2 = 0 \tag{1.16}$$

For a periodic (but not monochromatic) vector potential with period $T = 2\pi/\omega$, the solutions t_s to 1.16 are used to determine $M_{\mathbf{p}}$ [23, 46].

$$M_{\mathbf{p}} \propto \sum_n \delta\left(\frac{\mathbf{p}^2}{2m} + E_{IP} + U_p - n\omega\right) \times \sum_s \left(\frac{2\pi i}{S''_{\mathbf{p}}(t_s)}\right)^{1/2} e^{i[E_{IP}t_s + S_{\mathbf{p}}(t_s)]} \langle \mathbf{p} - e\mathbf{A}(t_s) \mid H_I \mid \psi_0 \rangle, \tag{1.17}$$

where $S''_{\mathbf{p}}$ is the second time derivative of the action. The sum over s includes all solutions of Eq. 1.16 within one period of the field.

Success in describing the highly non-linear processes of ATI and HHG lies in being able to redefine the $H^0(t)$ for different regimes: first by the Coulomb-free electron then by the parent atom.

1.3.2 Few-body *ab initio* methods

Floquet

The Floquet method [33] is a partial wave expansion that makes use of the periodicity of the laser field to simplify the wave function

$$\Psi(\mathbf{r}, t) = \frac{1}{r} \sum_{n\ell m} F^{(i)}_{n\ell m}(r) Y_{\ell m}(\mathbf{\Omega}) \exp^{-iEt + in(\omega t + \delta)} \tag{1.18}$$

where E is called the quasi-energy of the system. By applying this expansion, the solution of the time-dependent problem has been converted into a time independent system of coupled algebraic equations. The Floquet approach is most efficient for long pulses which need relatively few partial wave terms.

R-Matrix

The R-Matrix method [10, 37] partitions configuration space into two or more regions based on different physical processes. The basis is chosen to fit the physical behavior e.g. a linear combination of atomic orbitals to describe the interior electrons and

plane waves to account for ionization. The representations of the wave function in each region are connected by the R-matrix which is defined on the common boundary.

Close-coupling method

Close-coupling [50, 17] is the most popular *ab initio* method for solving the full two-electron TDSE. Its success lies in its ability to include the cylindrical symmetry imposed by a linearly polarized laser reducing the 6D electron system to 5D one through the use of coupled spherical harmonics

$$\mathcal{Y}_{\ell_1\ell_2}^{LM}(\mathbf{\Omega_1}, \mathbf{\Omega_2}) = \sum_{m_1 m_2} \langle \ell_1 m_1 \ell_2 m_2 \mid \ell_1 \ell_2 LM \rangle Y_{m_1}^{\ell_1}(\mathbf{\Omega_1}) Y_{m_2}^{\ell_2}(\mathbf{\Omega_2}). \tag{1.19}$$

where $\langle \ell_1 m_1 \ell_2 m_2 \mid \ell_1 \ell_2 LM \rangle$ is the Clebsch-Gordon coefficient, L is the total angular momentum, M is its z-axis projection, and ℓ_1 & ℓ_2 and m_1 & m_2 are the single-electron total angular momentum and z-axis projection respectively. The wave function is represented as

$$\Psi(t) = \sum_{LM} \sum_{\ell_1\ell_2} \chi_{\ell_1\ell_2}^{LM}(r_1, r_2) \mathcal{Y}_{\ell_1\ell_2}^{LM}(\mathbf{\Omega_1}, \mathbf{\Omega_2}) \tag{1.20}$$

where $\chi_{\ell_1\ell_2}^{LM}(r)$ are the numerical, radial wave functions which use finite elements, a discrete variable representation, or radial B-splines.

S-Matrix

An alternate formulation of S-matrix theory [6] accommodates multiple particles. The S-matrix expansion is based on a partition of the total Hamiltonian into a reference Hamiltonian H^0 and the interaction potential V.

$$H(t) = H^0(t) + V(t) \tag{1.21}$$

The TDSE is then rewritten as an integral equation

$$| \Psi(t)\rangle = |\phi(t)\rangle + \int_{t_i}^{t_f} dt' G(t,t')V(t')|\phi(t)\rangle \tag{1.22}$$

where $(t_f > t_i)$ $G(t,t')$ is the total Green's function satisfying

$$\left[i\frac{\partial}{\partial t} - H(t)\right]G(t,t') = \delta(t-t'), \tag{1.23}$$

and $\phi(t)$ is a solution of the Schrödinger equation of the unperturbed Hamiltonian $H_0(t)$.

$$\left[i\frac{\partial}{\partial t} - H^0(t)\right]|\phi(t)\rangle = 0 \tag{1.24}$$

The free particle Green's function

$$G_0(t,t') = -i\theta(t-t') \int d\mathbf{p} \mid \phi_{\mathbf{p}}(\mathbf{r})\rangle \exp\left[-\frac{i}{2}\int_{t'}^{t}\left(\mathbf{p} - \frac{\mathbf{A}(t'')}{c}dt''\right)^2\right]\langle\phi_{\mathbf{p}}(\mathbf{r}) \mid \tag{1.25}$$

is written as linear combination of H_0's eigenstates indexed by $\mathbf{p}$. The "total" Green's function is constructed from the interaction potential.

$$G(t,t') = G_0(t,t') + \int_{t_i}^{t_f} dt' G_0(t,t')V(t')G(t,t') \tag{1.26}$$

Since G appears on both sides of the above equation, some clarification is in order. Consider the wave function,

$$|\Psi(t)\rangle = |\phi(t)\rangle + \int_{t_i}^{t_f} dt_1 G_0(t,t_1)V(t')|\phi(t)\rangle \tag{1.27}$$
$$+ \int_{t_i}^{t_f}\int_{t_i}^{t_f} dt_2 dt_1 G_0(t,t_2)V(t_2)G(t_2,t_1)V(t_1)|\phi(t)\rangle$$

in addition to the initial state $|\phi(t)\rangle$, a first-order scattering term is present. One can imagine the far right wave function ϕ scattering off of V at t_1 and then propagating for the remainder of the simulation. Similarly, when Eq. 1.25 is substituted into Eq.

18

1.27, second-order scattering events can be imagined as ϕ scattering at t_1, propagating until a second (nucleus/electron) scattering at t_2, and continuing until the end of the simulation. Thus, increasingly complex events can be modeled with better approximations of G: e.g. Eq. 1.25 being substituted into Eq. 1.27 and accounting for third-order scattering events.

In few-electron calculations a variety of ionization mechanisms are present. The series nature of the S-matrix wave function lends itself to Feynman-like diagrams. Thus, one can taylor a simulation to compare different ionization mechanisms.

1.3.3 Many-body methods

Hartree-Fock

This section is adapted from Schneider [54]. Hartree-Fock (HF) is capable of handling hundreds of electrons. Each interacts with the average field of the remaining electrons. In this mean field, individual electron-electron interactions are lost. The difference between HF and reality is called *electron correlation*.

First, a basis set is chosen. Then each electron is adjusted in the average field of the remaining electrons until an equilibrium or Self Consistent Field (SCF) is established. The resulting wave function is an antisymmetric product of single particle orbitals and can be described by a single Slater determinant of the original basis.

$$\Psi_{HF} = |\phi_1 \phi_2 \cdots \phi_N| \tag{1.28}$$

The computational cost of a system described by N basis functions scales as $\mathcal{O}(N^4)$.

Consider an H_2 molecule represented by two orbitals

$$\Psi_{HF}(1,2) = |1s_A(1)1s_B(2)| \tag{1.29}$$

where the nuclei are labeled A and B. This antisymmetric product

$$\Psi_{HF}(1,2) = -1s_A(1)1s_B(2) - 1s_B(1)1s_A(2) \qquad (1.30)$$
$$+ 1s_A(1)1s_A(2) + 1s_B(1)1s_B(2)$$

is a combination of covalent (top line) and ionic (bottom line) terms. By construction, the Slater determinant contains an equal mixture of covalent and ionic terms. At equilibrium, this might be a reasonable description of the H_2 molecule; however, if one is interested in molecular disassociation, this becomes an unreasonable approximation as the internuclear separation approaches infinity. With increasing separation, the HF energy becomes higher than the true bond energy. This breakdown of HF is due to the limitation of a single determinant and serves as an example of a *static correlation* problem.

MCSCF

The failure of HF in describing the bond-breaking situations of H_2 can be remedied by the inclusion of another determinant.

$$\Psi_{MCSCF}(1,2) = t\Psi_{HF}(1,2) + t'\Psi'_{HF}(1,2) \qquad (1.31)$$

When the variational parameters (t and t') are included with the orbital coefficients in the energy minimization, the Multi-Configuration Self-Consistent Field (MCSCF) calculation includes electron correlation. The strength of MCSCF lies in using a minimal basis to account for correlation energy in a ground state configuration.

Dynamic correlation occurs between electrons away from their equilibrium position: excited state interactions, transition energies, and ionization. Unlike static correlation dynamic correlation is not localized in a few intuitive Slater determinants; thus, MCSCF fails at these tasks. A systematic combination of many different Slater determinants is the standard way to account for dynamic correlation.

CI

Configuration Interaction (CI) is a systematic variational combination of excited Slater determinants in the wave function

$$\Psi_{CI} = t\Psi_{HF} + \sum_{ia} t_i^a \Psi_i^a + \sum_{ijab} t_{ij}^{ab} \Psi_{ij}^{ab} + \cdots \qquad (1.32)$$

where ij represent the occupied orbitals, ab represent virtual orbitals, and the t coefficients are the variational parameters. The systematic inclusion of *every* Slater determinant captures the dynamic correlation available in the chosen basis. This is less than the full dynamic correlation energy. When using CI, one must play the educated guessing game of matching a sufficiently large basis with the appropriate number of excitations, to achieve convergence at minimal computational expense.

Chapter 2

Fundamentals of laser-atom interactions

2.1 The semi-classical approximation

Mittleman's Introduction to the Theory of Laser-Atom Interactions [41] and Bransden and Joachain's Physics of Atoms and Molecules [9] served as sources for this chapter. Lasers distinguish themselves from other forms of radiation by their high intensity, monochromaticity, and coherence. An infrared laser with $\lambda = 800nm$ corresponds to a frequency of $\omega = 1.5eV$; even at a weak intensity of $10^{-3}W/cm^2$ in a modest volume of $1cm^3$ has about 10^6 photons.

$$N = \frac{\text{energy flux}}{\hbar\omega}\frac{V}{c} = \frac{10^{-3}W/cm^2}{1.5eV}\frac{1eV}{1.6 \times 10^{-19}Ws}\frac{1cm^3}{3 \times 10^{10}cm/s} = 1.4 \times 10^6 \quad (2.1)$$

This large number means that the laser field will be unaffected by the absorption of a few photons and can be described by the classical electric field $\mathbf{E}$ or the vector potential $\mathbf{A}$ which are related as follows

$$\mathbf{E} = -\frac{\partial\mathbf{A}}{\partial t} \qquad (2.2)$$

Lagrangian mechanics are employed in construction the Hamiltonian $\mathscr{H}$. The canonical momentum $\mathbf{p}$ is not proportional to the time derivative of the canonical coordinate i.e. $\dot{\mathbf{q}} = \mathbf{v} \neq \mathbf{p}/m$.

$$\mathscr{L} = T - V = \frac{mv^2}{2} - q\big(\varphi - \mathbf{v} \cdot \mathbf{A}\big) \tag{2.3}$$

$$\mathbf{p} = \frac{\partial \mathscr{L}}{\partial \dot{q}} = m\mathbf{v} + q\mathbf{A} \tag{2.4}$$

$$\mathscr{H} = \dot{\mathbf{q}} \cdot \mathbf{p} - \mathscr{L} = \frac{mv^2}{2} + q\varphi = \frac{1}{2m}\big(\mathbf{p} - q\mathbf{A}\big)^2 + q\varphi \tag{2.5}$$

This is the origin of the Hamiltonian for a charged particle in an electric field.

2.2 The dipole approximation

For a given frequency ω and electric field $\mathscr{E}_0$ a laser can be described by the vector potential

$$\mathbf{A} = \frac{\mathbf{E}}{i\,\omega}e^{i(\mathbf{k}\cdot\mathbf{r}-\omega t)} = \frac{\mathbf{E}}{i\,\omega}e^{-i\omega t}\left(1 + i\mathbf{k}\cdot\mathbf{r} - \frac{1}{2}(\mathbf{k}\cdot\mathbf{r})^2 + ...\right) \tag{2.6}$$

$$= \frac{\mathbf{E}}{i\,\omega}e^{-i\omega t} + \mathcal{O}(\mathbf{k}\cdot\mathbf{r}) \tag{2.7}$$

When the spatial extent of the system is much less than the wavelength of the laser $\mathbf{r} \ll \mathbf{k}$, the first term in the parenthesis of Eq. 2.6 dominates the series. Dropping the spatially dependent powers of $(\mathbf{k}\cdot\mathbf{r})$ simplifies $\mathbf{A}$ and is the essence of the dipole approximation.

2.3 Gauge

2.3.1 Electromagnetic gauge

The representation of the Lorentz force by the electromagnetic potentials φ and $\mathbf{A}$ (rather than the $\mathbf{E}$ and $\mathbf{B}$ fields) is subject to a choice of gauge Λ_{EM}.

$$\mathbf{A}' \to \mathbf{A} + \nabla \Lambda_{EM} \tag{2.8}$$

$$\varphi\,' \to \varphi - \frac{\partial \Lambda_{EM}}{\partial t}$$

$\Lambda_{EM} = 0$ is an obvious first choice for the field gauge; this yields the Hamiltonian

$$\mathscr{H} = \frac{p^2}{2m} - \frac{q}{m}\mathbf{p} \cdot \mathbf{A} + \frac{q^2}{2m}A^2 + q\varphi \tag{2.9}$$

where φ represents the electrostatic potential of the atom and $\mathbf{A}$ describes the laser field. It is convenient to define H_0 as the stationary Hamiltonian and H_I as the interaction Hamiltonian.

$$H_0 = \frac{p^2}{2m} + q\,\varphi \tag{2.10}$$

$$H_I = -\frac{q}{m}\mathbf{p} \cdot \mathbf{A} + \frac{q^2}{2m}A^2 \tag{2.11}$$

2.3.2 Atomic units

It is advantageous to adopt atomic units for two reasons. First, they set many of the above constants to unity which simplifies the equation. Second, their units make it easy to recognize possible approximations. m_e the electron charge $|e|$, and the Plank constant $\hbar$ are equal to unity. The atomic unit of energy (Hartree) is exactly twice the ground state of hydrogen (1 Hartree = 27.2 eV). The unit of time, 24.2 as (as = 10^{-18} sec), is defined as the time it takes an electron in the ground state of hydrogen to orbit one atomic unit of distance. The unit of electric field $\mathscr{E}_0 = 5.14 \times 10^{11} V/m$ is

defined as that experienced by an electron in the ground state of the hydrogen atom, and the atomic unit of intensity is $3.5 \times 10^{16} W/cm^2 = c\mathscr{E}_0^2/8\pi$. Atomic units will be used unless labeled otherwise.

2.3.3 Quantum gauge

The observable behavior of an electrostatic system is not affected by the choice of the electromagnetic gauge Λ_{EM} in Eq. 2.8. Similarly, the observables of quantum mechanical system are independent of an alteration of the quantum mechanical gauge Λ_{QM}.

$$\Psi \rightarrow \exp\left[-i\Lambda_{QM}t\right]\Psi' \tag{2.12}$$

This unitary transformation is an opportunity to simplify the Hamiltonian.

$$i\frac{\partial \Psi'}{\partial t} = \left(\exp\left[i\Lambda_{QM}\right]\mathscr{H}\exp\left[-i\Lambda_{QM}\right] - \dot{\Lambda}_{QM}\right)\Psi' \tag{2.13}$$

through the time derivative of $\dot{\Lambda}_{QM}$.

2.3.4 Velocity gauge

When the $\mathscr{E} \ll \mathscr{E}_0$ the A^2 term in the Hamiltonian (Eq. 2.9) becomes negligible. A suitable choice of gauge,

$$\Lambda_{EM} = 0 \qquad \Lambda_{QM} = \frac{1}{2}\int^t dt' A^2(t') \tag{2.14}$$

known as the velocity gauge, removes it from the Hamiltonian.

$$\mathscr{H} = \frac{p^2}{2} - \mathbf{p}\cdot\mathbf{A}(t) + \varphi. \tag{2.15}$$

$$H_V = -\mathbf{p}\cdot\mathbf{A}(t) \tag{2.16}$$

2.3.5 Length gauge

Our scheme uses the length gauge, another Hamiltonian used to describe a laser field. When

$$\Lambda_{EM} = -\frac{\mathbf{r} \cdot \mathbf{E}}{i\,\omega}\, e^{-i\omega t} \qquad \Lambda_{QM} = 0, \tag{2.17}$$

the vector field transformation

$$\mathbf{A}' \rightarrow \mathbf{A} + \nabla \Lambda_{EM} = \frac{\mathbf{E}}{i\,\omega} e^{-i\omega t} - \frac{\mathbf{E}}{i\,\omega} e^{-i\omega t} = 0 \tag{2.18}$$

removes the $\mathbf{p} \cdot \mathbf{A}(t)$ term from the Hamiltonian (Eq. 2.9) while the electric potential transformation

$$\varphi' \rightarrow \varphi - \frac{\partial \Lambda_{EM}}{\partial t} = \varphi + \mathbf{r} \cdot \mathbf{E}\, e^{-i\omega t} \tag{2.19}$$

adds the electric field which allows us to specify the exact form of the electric field

$$\mathbf{E}(t) = E \sin^2(\omega t/2n_{cy}) \cos(\omega t + \varphi_{CE})\, \hat{\mathbf{z}} \qquad 0 \le t < \frac{2\pi\, n_{cy}}{\omega} = T \tag{2.20}$$

in the length gauge Hamiltonian

$$\mathscr{H} = \frac{p^2}{2m} + \varphi(\mathbf{r}) + \mathbf{r} \cdot \mathbf{E}(t) \tag{2.21}$$

$$H_L = \mathbf{r} \cdot \mathbf{E}(t). \tag{2.22}$$

2.4 Explicit time evolution

The general, time-evolution operator

$$\mathcal{U}(t + \Delta t, t) = \mathcal{T} \exp\left(-i \int_t^{t+\Delta t} \mathscr{H}(t')dt' \right) \tag{2.23}$$

26

gives a formal solution of the TDSE

$$\Psi(t) = \prod_i \mathscr{U}(t_i + \Delta t, t_i)\Psi(t_0)$$

$$= \mathcal{T}\prod_i \exp\left(-i\int_{t_i}^{t_i+\Delta t} \mathscr{H}(t)dt\right)\Psi(t_0). \qquad (2.24)$$

Above, $\mathcal{T}$ represents the time-ordering operator for the exponentials with non-commuting arguments, e.g. $\left[\mathscr{H}(t_1), \mathscr{H}(t_1)\right] \neq 0$. Generally the Dyson series is used for a solution; however, we assume the laser field is constant over a small interval of time Δt giving

$$\mathscr{U}(t + \Delta t, t) = \exp\left(-i\mathscr{H}(t)\Delta t\right) \qquad (2.25)$$

in this approximation

$$\Psi(t) = \prod_i \mathscr{U}(t_i + \Delta t, t_i)\Psi(t_0) = \prod_i \exp\left(-i\mathscr{H}(t)\Delta t\right)\Psi(t_0). \qquad (2.26)$$

Eq. (2.25) is transitive

$$\mathscr{U}(t + 2\Delta t, t) = \mathscr{U}(t + 2\Delta t, t + \Delta t)\mathscr{U}(t + \Delta t, t) \qquad (2.27)$$

and unitary

$$\mathscr{U}(t + \Delta t, t)^\dagger = \mathscr{U}(t + \Delta t, t)^{-1} \rightarrow \qquad (2.28)$$

$$\langle\Psi(t) \mid \Psi(t)\rangle = \langle\Psi(t + \Delta t) \mid \Psi(t + \Delta t)\rangle \quad \forall t, \Delta t. \qquad (2.29)$$

27

Chapter 3

Methods

MADNESS: a Multiresolution ADaptive Numerical Environment for Scientific Simulation is the framework with which our time evolution scheme is developed. At the highest level MADNESS represents functions and their operations in a multiresolution basis. Consider the approximation of the black function in Fig. 3.1a. Dividing the domain and giving each half a set of basis functions, as shown in Fig. 3.1b yields a better approximation. This is repeated recursively until the desired accuracy is achieved across the domain.

Figure 3.1: The bold curve is a function $f(x)$ to be approximated by the gray curve.

In 2002, Alpert et. al. [3] outlined the application of the Multiwavelet formalism to an adaptive solution of a partial differential equations. In 2004, Harrison et. al. [60, 25] published the results of the initial application to Hartree-Fock and density functional theory. Other developers have since joined the project extending application domain and enhancing the efficiency.

Section 3.1 explains the algorithm from a computational chemistry perspective. This is followed by a detailed explanation spatial representation in Section 3.2 and band-limited time evolution in Section 3.3. The implications band-limited propagator is discussed in Section 3.4. Finally, future work is outlined in Section 3.5.

3.1   MADNESS: computational introduction

In sharp contrast to most other computational tools in chemistry and physics, our computational framework MADNESS (Multiresolution ADaptive NumErical Scientific Simulation) [60, 25, 16, 26] does not have a fixed basis. The adaptive refinement automatically and dynamically changes to deliver the requested precision ϵ; this provides many advantages. The bound and free states are treated on an equal footing, the basis functions are only placed where needed, and it is not necessary to choose a basis in anticipation of the simulation results. Efficient computation, however, demands the use of finite precision (to terminate the adaptive refinement); understanding and controlling the effects of this finite precision is central to effective computation within MADNESS. Multiresolution analysis [3] provides efficient representations of many integral operators and algorithms that satisfy the requested precision by adaptive refinement (or truncation of fine-scale detail).

At the level of most scientific applications, MADNESS [25] provides a "basis-free" model of computation for which the only control parameter is, in principle, the desired precision of computation or truncation threshold ϵ. In practice, efficient computation demands that the order of the basis k be increased as the precision is increased (lower

ϵ) in order to decrease the effective bandwidth of integral operators (see section **??** for discussion on time evolution).

Computation is expressed in terms of operators acting on functions and is usually very close to the equations that express the physics. For instance, given a six-dimensional wave function $\psi(\mathbf{r}_1, \mathbf{r}_2)$, the calculation two-electron energy

$$E = -\frac{1}{2}\langle\psi|\nabla^2 + V(r)|\psi\rangle + \langle\psi \mid \frac{1}{|\mathbf{r}_1 - \mathbf{r}_2|} \mid \psi\rangle \tag{3.1}$$

becomes the following C++ code.

```cpp
double ke = 0.0;
for (int axis=0; axis<NDIM;axis++) {
    functionT dpsi = diff(psi,axis);
    ke += inner(dpsi,dpsi);
}
operatorT G = CoulombOperator(k, rlo, thresh);
functionT rho = psi*psi;
double pe = inner(V,psi);
double twoe = inner(G(rho),rho);
double energy = -0.5*(ke + pe) + twoe;
```

MADNESS is built upon Message Passing Interface (MPI) that allows it to take advantage of multi-core architecture. The compact support of the wavelet formalism works well with parallel computer architecture that distributes a function's coefficients across multiple processors. This scaling allows larger functions (translating into higher accuracy) to benefit from the memory of tens of thousands of processors. Some operations, such as multiplication by a constant, benefit from linear scaling; non-local operations that require lots of interprocessor communication, such as Green's function convolution, do not scale as aggressively. In anticipation of scaling to tens of thousands of processors, MADNESS developers have used linearly scaling algorithms whenever possible. Extending an out-of-the-box, parallel interface coupled

with optimized algorithms to scientific programmers. A brief introduction to the key concepts in our adaptive numerical refinement follows directly.

In summary, most numerical schemes compute exactly (or to machine precision) within an approximate finite basis, whereas MADNESS computes to a finite precision within an effectively exact, infinite basis. The computational implementation in C++ is close to the problem domain.

3.2   Spatial representation

The multiresolution formalism is naturally suited for adaptive refinement. A mathematical explanation of the relationship between vector spaces and behavior of the wavelets allows an appreciation of the nature of MADNESS's efficiency.

3.2.1   The multiresolution formalism

Let $\mathbf{V}_n^k$ be the space of piecewise polynomial functions,

$\mathbf{V}_n^k = \{f : \text{the restriction of f to the interval } (2^{-n}\ell, 2^{-n}(\ell+1)), \text{ is}$
a polynomial of degree less than k, for $\ell = 0, ..., 2^n - 1$ and f vanishes
elsewhere $\}$

Members of V_n^k are of the form

$$f^n(x) = \sum_{i}^{2^n-1} \sum_{\ell}^{k-1} s_{\ell i}^n \, \phi_{\ell i}^n(x) \qquad s_{\ell i}^n = \int f(x) \, \psi_{\ell i}^n \qquad (3.2)$$

Note that each function in V_n^k can be represented in V_{n+1}^k, or stated another way

$$V_0 \subset V_1 \subset ... \subset V_{n-1} \subset V_n \subset ... L^2([-1, 1]). \qquad (3.3)$$

where L^2 is the set of continuous, square integrable functions with finite norm. It is useful to define another function space W_{n-1} as the difference $\ominus$ between two

consecutive function spaces V_n.

$$W_{n-1} = V_n \ominus V_{n-1} \tag{3.4}$$

$$V_n = V_0 \oplus W_1 \oplus ... \oplus W_{n-1} \tag{3.5}$$

$$V_n = V_0 \oplus (V_1 \ominus V_0) \oplus (V_2 \ominus V_1) \oplus ... \oplus (V_{n-1} \ominus V_n) \tag{3.6}$$

where $\oplus$ represents the union between two sets. The members of W_{n-1} are called wavelets, which like the scaling functions ψ, they have finite support and are discontinuous (cf. Fig. 3.2). Each scaling function has a corresponding wavelet function (see panel in Fig. 3.2). Thus, a mathematically equivalent representation of f with the wavelet functions

$$f^n(x) = \sum_{\ell}^{k-1} s_{\ell 0}^0 \, \phi_{\ell 0}^0(x) + \sum_{i}^{2^n-1} \sum_{\ell}^{k-1} d_{\ell i}^n \, \phi_{\ell i}^n(x) d_{\ell i}^n = \int f(x) \, \psi_{\ell i}^n \tag{3.7}$$

provides a more efficient basis for certain operations (like the inner product) due to the following orthogonality relations.

$$\begin{aligned} \int \phi_{\ell i}^n(x)\phi_{\ell' i'}^{n'}(x) \, dx &= \delta_{nn'}\delta_{\ell\ell'}\delta_{ii'} \\ \int \psi_{\ell i}^n(x)\psi_{\ell' i'}^{n'}(x) \, dx &= \delta_{nn'}\delta_{\ell\ell'}\delta_{ii'} \\ \int \phi_{\ell i}^n(x)\psi_{\ell' i'}^{n'}(x) \, dx &= 0 \quad \text{if } n > n' \end{aligned} \tag{3.8}$$

3.2.2   Spatial representation in MADNESS

Multiresolution analysis within a multiwavelet basis [3] is best explored with a 1D function f. At the coarsest level (n=0), f is represented by a linear combination of scaling functions

$$\phi_i(x) = \begin{cases} \sqrt{2i+1} \, P_i(2x-1) & x \in [0,1] \\ \\ 0 & \text{otherwise} \end{cases}$$

32

where $P_i(x)$ are the Legendre polynomials. These parent scaling functions (n=0) are shifted and dilated as f is refined. The first level of refinement (n=1) splits the domain and represents each side with an independent set of k scaling functions.

$$\phi_{i\ell}^n(x) = 2^{n/2}\phi_i(2^n x - \ell) \tag{3.9}$$

At level n of refinement there are 2^n subdomains that are indexed by ℓ.

In MADNESS, each subdomain of f is adaptively refined until it satisfies the requested numerical tolerance (ϵ). f is represented (see Fig. 3.2) by the subdomains (boxes) that cover the original domain.

$$f^{(\epsilon)}(x) = \sum_{n\ell}^{boxes} \sum_i^{k-1} s_{i\ell}^n \, \phi_{i\ell}^n(x) \qquad s_{i\ell}^n = \int f(x)\,\phi_{i\ell}^n \, dx. \tag{3.10}$$
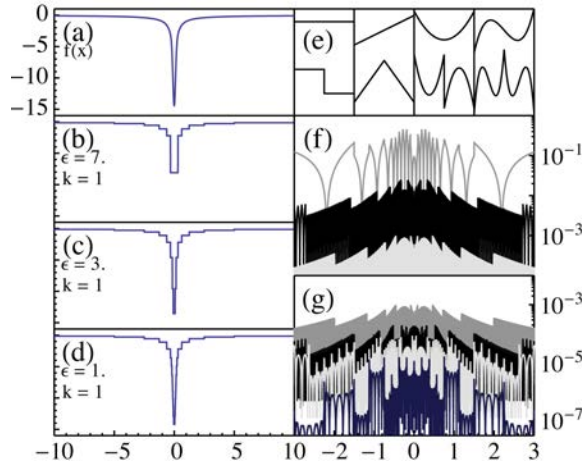
Figure 3.2: The function f to be approximated is in (a). Panels (b) - (d) show function refinement at k = 1 with successively smaller numerical thresholds (ϵ). In (e) the first four scaling functions from Eq. 3.10 are shown above their corresponding wavelet from Eq. 3.11. The absolute value of the refinement error in is shown in (f) with k = 1 and $\epsilon = 10^{-1}, 10^{-3}, 10^{-5}$ and in (g) with $\epsilon = 10^{-5}$ and k = 1, 2, 3, 6.

Each scaling function $\phi_{i\ell}^n(x)$ (see Fig. 3.2(e) upper row) has a corresponding wavelet function $\psi_{i\ell}^n(x)$ (Fig. 3.2(e) lower row). This provides a second mathematically

equivalent representation of f

$$f^{(\epsilon)}(x) = \sum_{i=0}^{k-1} s_{i\ell}^0 \, \phi_{i\ell}^0(x) + \sum_{n\ell}^{boxes} \sum_{i=0}^{k-1} d_{i\ell}^n \, \psi_{ij}^n(x) \qquad d_{i\ell}^n = \int f(x) \, \psi_{i\ell}^n \, dx. \qquad (3.11)$$

The wavelets provide a more efficient basis for certain operations (like the inner product) due to the following orthogonality relations in Eq. 3.8.

There exists a fast transform between the scaling function representation in Eq. 3.10 and wavelet representation in Eq. 3.11 much like the fast Fourier transform. This dual representation is analogous to the real/momentum space representation.

Function refinement, the recursive subdivision of the domain, continues until the difference coefficients satisfy the refinement criteria.

$$||d_\ell^n||_2 = \sqrt{\sum_i |d_{i\ell}^n|^2} \leq \epsilon \qquad (3.12)$$

The refinement is deepest in regions where f is not smooth (see Fig. 3.2). The approximation error for a locally smooth function scales as $\mathcal{O}(2^{-nk})$ while the error near a discontinuity as $\mathcal{O}(2^{-n})$. A typical, low-accuracy run of the TDSE for the hydrogen atom ($k = 12$, $\epsilon = 1 \times 10^{-5}$, and $\xi = 0.3$) (see Section 3.4.1) refines to a depth of $n = 9$ while a high-precision run ($\xi = 0.05$, $k = 24$ and $\epsilon = 1 \times 10^{-7}$) refines to $n = 11$.

The Cartesian coordinate representation, while not necessary for simulation in MADNESS, carries many benefits. It is easy to extend a function to an arbitrary number of spatial dimensions while maintaining a consistent interface with the operators. Thus, the implementation of the 3D solution to the TDSE is only marginally more complicated than that of a 1D solution, and the extension of 3D atomic hydrogen to fixed nuclear H_2^+ was only a modification of the input file parameters. In Chapter 7, we provide preliminary results from a 4D representation of H_2^+ where the internuclear separation is treated on the same footing as the 3D electronic components. A 6D treatment of two-electron He, while more

computationally intensive, only requires the addition of an electron-electron repulsion term to the Hamiltonian.

In summary, the multiresolution formalism provides the illusion of a basis-free simulation by automating the extension or contraction of the basis through adaptive refinement. Most *ab initio* schemes compute matrix elements to machine precision within a fixed finite basis. MADNESS, however, computes to finite precision in a dynamically changing basis. Finally, the Cartesian framework of MADNESS is readily extendable to larger systems.

3.3 Time evolution

Time evolution in MADNESS is inseparable from a band limited momentum spectrum, for finite resources can not propagation dynamics of an unbounded function. After a general description of operator application, we will examine the time evolution operator and its implications.

3.3.1 The multiresolution formalsim

This section is adapted from [25]. Consider $T_n = P_n T P_n$, the projection of an operator T to be applied to f^n where P_n maps $f : L^2([0, 1]) \to V_n$. In one spatial dimension,

the elements of T are denoted by the transition matrix r_{lm}^n

$$\left(P_n f\right)(x) = \sum_{m=0}^{2^n-1} \sum_{j=0}^{k-1} s_{jm}^n \, \phi_{jm}^n(x) \tag{3.13}$$

$$\left(P_n T P_n f\right)(x) = \sum_{m=0}^{2^n-1} \sum_{j=0}^{k-1} \tilde{s}_{jm}^n \, \phi_{jm}^n(x) \tag{3.14}$$

$$\tilde{s}_{jm}^n = \sum_{m=0}^{2^n-1} \sum_{j=0}^{k-1} \left[r_{lm}^n\right]_{ij} s_{jm}^n \tag{3.15}$$

$$\left[r_{lm}^n\right]_{ij} = \int dx \int dy \, K(x-y) \, \phi_{il}^N(x) \, \phi_{jm}^n(y) \tag{3.16}$$

$$= \int dx \, \phi_{il}^n(x) \left(T\phi_{jm}^n\right)(x) \tag{3.17}$$

MADNESS's efficiency relies in a sparse representation of certain classes of operators.

Problem domains with details on different length scales stand to benefit from MADNESS which offers an adaptive sparse representation, eliminates basis set error, and scales aggressively on multiple processors. Most *ab initio* schemes compute matrix elements to machine precision within a fixed finite basis. The adaptive refinement of the multiresolution formalism in MADNESS computes to finite precision without basis error. More generally, MADNESS is designed as a computational framework to bridge the gap between the average scientist and the rapidly advancing computational frontier.

3.3.2   The propagator

For the temporal propagation of the TDSE (Eq. 2.21), we employ the fourth-order, gradient-corrected, symplectic propagator developed by Chin and Chen [11]. This time evolution operator

$$\mathcal{U}(dt,t) = e^{-i\frac{1}{6}V(t+dt)dt} e^{-i\frac{1}{2}\hat{T}dt} e^{-i\frac{2}{3}V(t+\frac{1}{2}dt)dt} e^{-i\frac{1}{2}\hat{T}dt} e^{-i\frac{1}{6}V(t)dt} + \mathcal{O}(dt^5) \tag{3.18}$$

reduces the error and total computational expense by allowing longer time steps than the second-order accurate, Trotter splitting [57]. The application of the exponentiated potential, in MADNESS, is simply function multiplication while the application of the exponentiated kinetic energy operator

$$\mathcal{U}_0(t) = e^{-i\frac{1}{2}\hat{T}dt} = e^{i\nabla^2 dt/2} \tag{3.19}$$

is an integral convolution. The potential-free Green's function of the TDSE (free-particle propagator) in D spatial dimensions

$$G_0(x,t) = (2\pi\,i\,dt)^{-D/2}e^{-\frac{x^2}{2idt}} \tag{3.20}$$

is applied to the wave function

$$\psi(x,dt) = \mathcal{U}_0(dt)\,\psi(x,0) = \int dx' G_0(x-x',dt)\psi(x',0). \tag{3.21}$$

advancing it forward in time.

Figure 3.3: (color online) (a) The real component of the 1D free particle propagator and (b) its band limited counterpart. The band limit (inset) in momentum space is the black line and the excluded Fourier components of the original function are dashed.

The unbounded spectrum of the kinetic energy operator $\mathcal{U}_0$ in Fig. 3.3(a) makes its complete computational representation impossible. However, we are not interested in representing the full operator, only the components necessary for the propagation of a band limited wave function. This is directly analogous to the upper energy limit on a uniform grid. The band limit is applied by transforming the full G_0 to momentum space (see inset in Fig. 3.3(b)), multiplying by a band limiting filter, and transforming back to real space (Fig. 3.3(b)). The band limited G_0 is bounded in real space and momentum space.

The discontinuous, spectral element basis is a computationally convenient alternative to the finite element or finite difference methods. Continuity emerges (within finite precision) with the application of an appropriately constructed integral or differential operator [3] as is the case with the stencils used in finite difference methods. Nevertheless, the adaptive, discontinuous, polynomial basis unavoidably includes numerical, high frequency components even when representing smooth functions. The insensitivity of the band limited G_0 to this numerical noise preserves the integrity of the wave function.

Scattering off the Coulomb singularity also allows arbitrarily high frequencies into the wave function. These legitimate, physical frequencies would introduce propagation error upon application of the band limited G_0. We prevent this error by band limiting the nuclear potential (see Sec. 3.4.1) to allow exact propagation. This is accomplished by smoothing the singularity at a closest scattering distance, which prevents high frequencies from entering the system. The cutoff parameter (ξ) controls the depth of the potential, the band limit, and the complexity of the simulation (see Sec. 4.1).

In addition to increasing the size of the wave function, the fine spatial variations associated with high frequencies require an impractically small time step. The TDSE is limited by a Courant-Friedrichs-Lewy-like [42] condition ($dt \propto \Delta x^2$) where the critical time step

$$dt_{crit} \simeq 2\pi/c^2 \propto (\Delta x)^2 \propto \xi^2 \tag{3.22}$$

38

where c is an empirically estimated band limit and Δx is the smallest mesh spacing controlled by ξ the potential smoothing parameter.

The application of the G_0 (see Fig. 3.3) is the most computationally intensive step of time evolution and efficiency hinges on its separability. While computer memory limits the size of the solution domain in fixed grid schemes, in MADNESS, memory limits the total complexity of the wave function. Massively-parallel, distributed-memory computers replace the memory constraint by a communication bandwidth limit. For a sufficiently large number of computational nodes, the convolution of G_0 is bottlenecked by interprocessor communication. The application cost of a general D dimensional convolution of a wave function with N coefficients scales as $\mathcal{O}(N^{2D})$. A 3D convolution $G_0(x, y, z, x', y', z') * \psi(x, y, z)$ requires six spatial indices. MADNESS takes advantage of the separable nature of the Gaussian form of G_0 (see Eq. 3.20) to accomplish the time evolution of a higher dimension system by repeated application of the $1D$ propagator

$$\prod_i G_0(x_i, x_i') * \psi(x, y, z) \qquad x_i \in (x, y, z) \tag{3.23}$$

which scales as $\mathrm{O}(N^{D+1})$. The reduced data transfer enables the time evolution of higher dimension systems. Details concerning the choice of the frequency windowing function, parametrization of the effective band limit, and accurate application of this oscillatory operator are found in the MADNESS implementation notes [26].

In summary, successful time evolution of a multiresolution wave function hinges on the band limit. First, it allows a multiresolution representation of G_0 by bounding its size. It allows a reasonable time step by quenching the high frequency noise endemic in the multiresolution wavelet representation. The band limit is controlled by the cut parameter ξ which confines the Coulomb singularity removing high momentum components and their associated propagation error. Finally, the separated nature of G_0 allows robust scaling on distributed memory computers.

3.4 Implications of the band-limit

3.4.1 Model potential

Since our eventual objective is the treatment of a general polyatomic systems without symmetry, we cannot rely on the Jacobian of special coordinates to exactly represent the Coulomb singularity in an integrable fashion. Thus, we use a smoothed approximation successfully employed in Hartree-Fock and density functional computations [25] to model a nuclear potential of charge Z (see Fig. 3.2(a)).

$$V_{model}(r) = \frac{\text{erf}(r)}{r} + \frac{e^{-r^2}}{\sqrt{\pi}} \qquad (3.24)$$

The coefficient of the Gaussian term is chosen so that the mean error is zero.

$$\int_0^\infty r^2 \left(V_{model}(r) - \frac{1}{r} \right) dr = 0 \qquad (3.25)$$

The depth of the model potential

$$V_\xi(r) = \frac{Z}{\xi} V_{model}(\frac{r}{\xi}) \qquad (3.26)$$

controls the maximum momentum component allowed in the wave function and is controlled by the cut parameter ξ. The band limit $c = 5/\xi$ (shown in the inset of Fig. 3.2(b)) has been empirically determined. The coarsest potential ($\xi = 0.3$) agrees with the Coulomb function to machine precision when $r > 2$. Smaller ξ produce an arbitrarily accurate agreement.

$$\lim_{\xi \to 0} V_\xi(r) = -\frac{Z}{r} \qquad (3.27)$$

Since rescattering is understood to be sensitive to the finest length scales [21], we emphasize the importance of the ξ convergence study in Section 4.1.

3.4.2 The initial eigenstate

It is desirable to begin the simulation with a stationary state of V_ξ. The initial Coulomb eigenstate is relaxed into an eigenstate of the model potential through the following self-consistent solution.

$$\psi(\mathbf{r}) = \left(-\tfrac{1}{2}\nabla^2 - E \right)^{-1} V_\xi(r)\, \psi(\mathbf{r}) \tag{3.28}$$

3.4.3 Eigenfunctions of the model potential

While the spatial resolution and time propagation are directly generalized to 3D, projection onto the bound and scattering states is unique to the geometry of each system. Analytic eigenfunctions make the hydrogenic systems a natural test case. The ionization spectrum was calculated by projecting the wave function onto the incoming spherical wave eigenstates [34] of the field-free Coulomb potential

$$
\begin{aligned}
\phi_{\mathbf{q}}^{(-)}(\mathbf{r}) \;=\;& (2\pi)^{-3/2} e^{\pi\eta/2} \\
&\times \Gamma\!\left(1 + i\eta \right) e^{i\mathbf{q}\cdot\mathbf{r}} \\
&\times {}_1F_1\!\left(-i\eta, 1, -iqr - i\mathbf{q}\cdot\mathbf{r} \right)
\end{aligned}
\tag{3.29}
$$

for nuclear charge Z and momentum of magnitude q, $\eta = Z/q$. These Coulomb scattering states are momentum normalized $\langle\, \phi_{\mathbf{q}'}^{(-)} \mid \phi_{\mathbf{q}}^{(-)} \,\rangle = \delta^3(\mathbf{q}' - \mathbf{q})$.

The softening of the Coulomb potential's singularity in Eq. 3.28 implies the Coulomb eigenstates are not eigenfunctions of the new model potential and have a non-zero overlap with initial state. Since the eigenstates of V_ξ are too expensive to compute, we remove the non-physical overlap between the Coulomb eigenstates and the initial state of the model potential.

$$P_{n\ell} = |\langle \phi_n \mid \psi(T) \rangle - \langle \phi_n \mid \psi(0) \rangle \langle \psi(0) \mid \psi(T) \rangle|^2 \qquad (3.30)$$

$$\Upsilon_{\mathbf{q}} = |\langle \phi_{\mathbf{q}} \mid \psi(T) \rangle - \langle \phi_{\mathbf{q}} \mid \psi(0) \rangle \langle \psi(0) \mid \psi(T) \rangle|^2 \qquad (3.31)$$

Eq. 3.30 describes this first order Gramm-Schmidt correction to the transition amplitudes as a change of basis. By removing the non-physical overlap between the analytic Coulomb eigenstates and the relaxed initial state of the model potential, we account for most of the discrepancy.

A partial integration of Eq. 3.31 provides the single differential probability distributions.

$$\frac{dP}{dE_f} = \int |\Upsilon_{\mathbf{q}}|^2 \, q \, d\Omega_q \qquad \frac{dP}{d\Omega} = \int |\Upsilon_{\mathbf{q}}|^2 q^2 dq \qquad \frac{dP}{dq} = \int |\Upsilon_{\mathbf{q}}|^2 q^2 d\Omega_q. \qquad (3.32)$$

where E_f is the kinetic energy of the photoelectron.

3.5 MADNESS: the future

MADNESS is a general numerical framework with a diverse and expanding portfolio of applications. Extension of time evolution has two possible routes. A large dimension wave function can capture electron correlation in few body systems. Another avenue is the development of an MCSCF (see Section 1.3.3) code to explore many-body dynamics.

3.5.1 High-dimensional wave functions

The AMO community is actively researching two-electron phenomena. The standard partial wave expansion for the wave function becomes inadequate to describe dynamics induced by circularly polarized laser pulses. A high dimension wave function in MADNESS would allow an easier representation of electron dynamics in these

pulse. A 7D wave function which including the internuclear separation in the two electron wave function is also a posibility.

3.5.2 MCSCF

A MCSCF implementation in MADNESS offers some unique benefits which would provide a more sustained impact due to the larger number of available systems e.g. the original problem of energetic carbon clusters. Consider a state in which two electrons occupy the same orbital i.e. a closed shell. This is often approximated by a single determinant since there is only one way two electrons can occupy a single orbital (with opposite spins). Upon excitation, one can see two ways of assigning electrons: $\alpha(1)\beta(2)$ or $\beta(1)\alpha(2)$. Thus, the simplest excited state is inherently multi-determinental.

A well designed MCSCF wave function can describe not just single but double and perhaps higher excitations. MADNESS's ability to treat both bound and free particle states equally makes it more straight forward than conventional MCSCF codes that need a different basis for bound and free particles: e.g. atom-centered Gaussians and plane waves.

Chapter 4

Convergence Study

In this section we study the effects of the sources of error in our numerical scheme: the numerical truncation threshold ϵ, the size of the time step dt, and the model potential cutoff parameter ξ. ϵ sets an upper bound on local error, and the time propagation error is proportional to the size and number of time steps. The cutoff parameter ξ determines the highest frequency allowed in the wave function by controlling the depth of the model potential and the band limit of the free-particle propagator.

4.1 Truncation Error

MADNESS's adaptive refinement allows arbitrary accuracy. However, finite resources impose a limit on the spacial refinement. This is realized by the truncation threshold ϵ which controls the local error. While the error in the wave function accumulates over multiple time steps potentially becoming greater than ϵ, some transition amplitudes achieve convergence *below* ϵ.

To determine the effect of ϵ on the system, we present the dynamics of the transition probabilities in Fig. 4.1 computed at three different truncation thresholds $\epsilon = 10^{-3}, 10^{-5}$, and 10^{-7}. Visually, the dynamics of the p-states and the 2s state are converged with $\epsilon = 10^{-3}$, whereas the 3s and 4s states require $\epsilon = 10^{-5}$ for convergence. Numerical error is also readily apparent for states with populations

Figure 4.1: (Color online) The bound state probabilities of He$^+$ as calculated in Eq. 3.30 for different values of the numerical truncation threshold ϵ (a) 10^{-3} (b) 10^{-5} (c) 10^{-7}. ϵ is represented by the horizontal dashed line. See labels in (a) for legend.

that continue to evolve after the end of the pulse, such as the f-states for $\epsilon = 10^{-3}$ and the g-states. Contrast the parallel curves within a converged angular momentum population with the behavior of an insufficiently converged group e.g. the f-states (Fig. 4.1(a) and (b)). Nevertheless, these states are within an order of magnitude of their final value at in Fig. 4.1(c). Thus, it is reasonable to conclude that the g-states in Fig. 4.1(c), while not converged, are within an order of magnitude of their converged value.

Figure 4.2: (Color online) The photoelectron ionization spectra for different values of thresh ϵ for (a) H ($\xi = 0.1$) and (b) He$^+$ ($\xi = 0.06$).

Fig. 4.2 shows the response of the photoionization momentum spectrum to ϵ. While the ionization of hydrogen is unaffected by ϵ, the weak ionization processes in

He$^+$ (Fig. 4.2(b)) are more sensitive and are misrepresented by the calculations when $\epsilon > 10^{-6}$.

Table 4.1 shows convergence trends in the transition probabilities of He$^+$. The one-photon transition probabilities to the 2p state is correct to three digits for $\epsilon = 10^{-3}$, and the two-photon transitions to the s and d states have errors on the order of 10%. An unconverged changes with successively smaller ϵ (see 5g) while a converged state oscillates about the correct value (see 2p and 2s). The 4f population is converged to 2 digits (2.0×10^{-8}). The 5g state, while not converged, is likely to be follow the pattern exhibited by the f-states: converging within an order of magnitude below where crossing is first exhibited 10^{-12}.

ϵ	1s	2s	2p	3d	4f	5g	ΣP_{bound}	P_{ion}
10^{-3}	0.974448	0.851×10^{-4}	0.021424	6.03×10^{-5}	5.6×10^{-7}	7×10^{-7}	0.999016	8.58×10^{-4}
10^{-4}	0.974507	1.059×10^{-4}	0.021432	6.52×10^{-5}	2.7×10^{-6}	2×10^{-7}	0.999108	8.01×10^{-4}
10^{-5}	0.974513	0.998×10^{-4}	0.021415	6.67×10^{-5}	4.2×10^{-8}	1×10^{-9}	0.999081	8.28×10^{-4}
10^{-6}	0.974512	0.999×10^{-4}	0.021422	6.72×10^{-5}	2.1×10^{-8}	2×10^{-10}	0.999060	8.43×10^{-4}
10^{-7}	0.974516	0.996×10^{-4}	0.021409	6.70×10^{-5}	2.0×10^{-8}	1×10^{-11}	0.999057	8.49×10^{-4}
ξ								
0.2	0.97678	1.158×10^{-4}	0.02520	6.96×10^{-5}	1.4×10^{-7}	7×10^{-8}	0.99890	8.97×10^{-4}
0.12	0.97319	1.017×10^{-4}	0.02244	6.80×10^{-5}	2.2×10^{-8}	6×10^{-12}	0.99898	9.21×10^{-4}
0.08	0.97421	1.004×10^{-4}	0.02166	6.74×10^{-5}	2.6×10^{-8}	3×10^{-11}	0.99905	8.59×10^{-4}
0.06	0.97452	0.996×10^{-4}	0.02141	6.70×10^{-5}	2.0×10^{-8}	1×10^{-11}	0.99906	8.49×10^{-4}
0.05	0.97460	0.997×10^{-4}	0.02135	6.71×10^{-5}	2.2×10^{-8}	6×10^{-12}	0.99909	8.38×10^{-4}

Table 4.1: Convergence of the transition probabilities of He$^+$ with $L \in [-1000, 1000]$. $\xi = 0.059$ for the threshold convergence ϵ study (top), and $\epsilon = 10^{-7}$ during convergence of ξ. The bound states were summed up to $n = 9$.

Time Step Error

At each time step (dt), error is accumulated from the size of the time step (ε_{dt}) and the truncation (ε_{trunc}) of the adaptive basis.

$$\varepsilon_{total} = \mathcal{O}(\frac{T\varepsilon_{trunc}}{dt}) + \mathcal{O}(\frac{T\varepsilon_{dt}}{dt}) \tag{4.1}$$

Figure 4.3: (Color online) The dynamic convergence of atomic hydrogen ($\xi = 0.2$, $\epsilon = 1 \times 10^{-5}$, and $dt_{crit} = 3.4 \times 10^{-3}$) with respect to the time step dt. The energy $\langle \hat{H} \rangle$ from Eq. 2.21 is shown in (a) along with its error at the end of the pulse in (b) is shown for different time steps. (c) shows the photoionization spectrum (see Eq. 3.32).

For large time steps ε_{dt} dominates, whereas, small dt implies many time steps and hence greater overall truncation error. Fig. 4.3(a) shows how different time steps affect the energy (expectation of the Hamiltonian) of hydrogen. At the end of the pulse, the relative error in Fig. 4.3(a) is shown in Fig. 4.3(b). For $dt/t_{crit} = 10$ we see a slight deviation in the energy which quickly diverges for larger values as ε_{dt} dominates. The photoionization peak in Fig. 4.3(c) is largely insensitive to dt. However, the peak of the smallest time step is slightly shifted to the right as ε_{trunc} accumulates after many time steps. Thus, the high-order symplectic integrator [11] is beneficial in enabling large time steps. The illustrations presented in this dissertation use $dt = 5t_{crit}$.

The Cutoff Parameter

The length scale on which the model potential is smoothed can be thought of as the closest scattering distance or cutoff parameter (ξ). In this section we probe the aberrations caused by its modification.

Fig. 4.4(a) shows the dynamic energy $\langle \hat{H} \rangle$ (where $\hat{H}$ is the Hamiltonian from Eq. 2.21) of hydrogen for different ξ. Smaller ξ lead to a lower, more accurate ground state energy E_0 which converges towards the analytic value of -0.5 in Fig. 4.4(d). The relative position of the transition energies in atomic hydrogen and the power spectrum of the laser (see the inset in Fig. 4.5(a)) predict single-photon ionization as the dominant process. As $\xi \to 0$, higher energy events are included, and the change in energy of the system

$$\Delta E = E(T) - E_0 \tag{4.2}$$

increases as $\xi \to 0$ (see Fig. 4.4(e)). This can also be seen for the total inelastic excitation

$$P(t) = 1 - |\langle \psi(0) \mid \psi(t) \rangle|^2 \tag{4.3}$$

(Fig. 4.4(h)) and total ionization (Fig. 4.5(a)).

Figure 4.4: (Color online) The dynamic convergence of H and He^+ with respect to the cut parameter ξ is shown for: the energy $\langle \hat{H} \rangle$ from Eq. 2.21 in (a) & (b) and the total inelastic excitation vs time from Eq. 4.3 in (c). Convergence of the ground state energy (d) & (f), the energy difference Eq. 4.2 in (e) & (g), and total inelastic excitation in (h) & (i) is shown as a function of ξ. The dotted line represents convergence within 1% of the extrapolated value.

While the convergence of hydrogen depends on high energy events, the convergence of He^+ is related to the stability of the ground state. In He^+ the ΔE (Fig. 4.4(g)), the total inelastic state excitation (Fig. 4.4(i)), and the photoionization (Fig. 4.5b) decrease as the transition energies shift towards a less intense region of the power spectrum as $\xi \to 0$. See Table 4.1 for a quantitative comparison.

We are interested in gauging the accuracy of our calculations. We generate a series of values with successively smaller ξ, interpolate between the lines, and mark the spot where the given quantity is within 1% of the final value (see the vertical dotted lines in Figs. 4.4(d)-(i)). The analytic value of the ground state energy offers unambiguous convergence, for hydrogen $\xi_{1\%} \approx 0.24$ (Fig. 4.4(d)) and for $He^+ \xi_{1\%} \approx 0.08$. Systems with a larger nuclear charge (Z) require a smaller ξ for the same accuracy. In previous work [25] the value of ξ required to obtain a fixed accuracy for the total energy was found to depend upon the atomic number Z according to $\xi \propto Z^{-5/3}$. The least converged value, ΔE in He^+ (Fig. 4.4(g), has $\xi_{1\%} = 0.07$ which is above the smallest value $\xi = 0.05$.

The effects of the smoothing can be seen in the oscillation of the z-dipole (Fig. 4.6). As ξ decreases from $0.2 \to 0.059$, larger transition energies have two effects. First, the dipole amplitude is damped: $|c_{2p}^{(0.059)}|^2 < |c_{2p}^{(0.2)}|^2$ (see Table 4.1). Second, the period of oscillation increases. While $t \in (10, 50)$, the dipole moment of $\xi = 0.2$ oscillates 9 times, while $\xi = 0.059$ oscillates 9.5 times. The $1s \to 2p$ transition energy $\omega_{12} = 2\pi/T = 1.496$, which deviates 0.2% from the analytic value of 1.5. The broadband laser pulse also excites the 3p state whose presence can be seen by the beats of the modulating envelope with a period only 13% away from the predicted value of 5/36: $\omega_{23} = 2\pi/T = 2\pi/(38 - 12) = 0.242$.

Box Size, Norm, and Timing Issues

The simulation box is a cube $[-L, L]^3$ deliberately chosen to be much larger than the final wave packet to avoid reflection or the need for absorbing boundary conditions. In MADNESS, the size of the *sparse* wave function ψ scales as $\mathcal{O}\big(\log(L)\big)$. The

Figure 4.5: (Color online) Convergence of the momentum distribution with respect to ξ for (a) H and (b) He^+. The relationship between the system's energy levels and the laser power spectrum is shown in the inset.

Figure 4.6: (Color online) The dipole moment $\langle z \rangle$ for He$^+$ as a function of time for ξ=0.2 and 0.059. The period changes with ξ, illustrating the shift in the bound state energies.

dense momentum eigenfunctions $\phi_{\mathbf{q}}^{(-)}(\mathbf{r})$, however, fill the entire simulation box scaling as $\mathcal{O}(L^3)$. For efficiency we compute $\phi_{\mathbf{q}}^{(-)}(\mathbf{r})$ in a reduced rectangular volume corresponding to the furthest extent

$$L_{small} = T\sqrt{2(n\omega - I_p)} \tag{4.4}$$

of an n-photon ionization for the duration of the pulse to escape from an ionization potential I_p. A 2 and 5 photon ionization of hydrogen corresponds to $L_{small} = 19$ and 35 in the current pulse. The largest reported relative error in the ionization probability $q^2 \, \Upsilon_{\mathbf{q}}$ is on the order of 10^{-5}. L_{small} will be a more important issue with infrared pulses in the tunneling regime where the electron is carried much further from the atom.

The loss of norm

$$\varepsilon_{norm}(t) = |1 - \langle \psi(t) \mid \psi(t) \rangle| \tag{4.5}$$

is due to several factors. First, the finite precision of the spatial representation of the wave function. Second, the repeated application of the band limited propagator. Split-operator methods of the TDSE are unitary and preserve norm. Nevertheless, norm is lost in by the truncation of the high-frequency coefficients. Typically this loss accumulates uniformly throughout the pulse ending with ε_{norm} approximately 10ϵ. Occasionally $\varepsilon_{norm}(T) < \epsilon$, while the worst deviation (atomic hydrogen with $\epsilon = 10^{-7}$, $\xi = 0.1$) had $\varepsilon_{norm}(T) \approx 100\epsilon$.

The application cost of G_0, which is related to its spatial extent and the size of the wave function, is affected by several interrelated parameters. Smaller ϵ directly increases the size of both G_0 and the wave function. Second, the cost is directly proportional to the number of time steps.

$$N_t = T/dt \propto T/\xi^2 \tag{4.6}$$

While dt and ξ directly affect N_t, they also add to the complexity of G_0. The electron propagates further during longer time steps; this increases the spatial extent of G_0 (L_{prop}). Smaller ξ increases the band limit c and includes faster momentum components enlarging L_{prop}.

$$L_{prop} \propto \xi^{-1} \propto c \propto q \tag{4.7}$$

On an 8 core Intel Xeon 2.9 GHz computer with 24 GB of shared memory, the time evolution of H in 3D ($L = 300, k = 12, \epsilon = 10^{-5}, dt = 5dt_{crit}, \xi = 0.2$) was accomplished in about an hour. Higher accuracy requires more memory, which becomes the limiting factor on larger calculations. He$^+$ ($L = 300, k = 24, \epsilon = 10^{-7}, dt = 4dt_{crit}, \xi = 0.059$) a typical high fidelity time evolution, took 46 hours running on a Cray XT5 running with 2,000 - 5,000 cores. Both time evolution and projection code realize performance increase (for sufficiently complex wave functions) through 12,000 cores.

4.1.1 Comparison to Prior Work

Pronin et al. [52] used perturbation theory to find the ionization of atomic hydrogen in a two-cycle pulse of the same frequency and intensity. However, their velocity gauge scheme applied the $\sin^2$ pulse envelope to the vector potential rather than the electric field which gave a very different photoionization spectrum. Grum-Grzhimailo et al. [24] noted this and ran a series of computations using a four-cycle laser pulse with peak intensity $1 \times 10^{15} W/cm^2$ and central frequency $\omega = 0.3$ (152 nm) to test the effect of the pulse envelope on the vector potential and electric field on the photoionization spectrum of atomic hydrogen. We reproduced this experiment for comparison purposes. We find only a minor aberation in the magnitude of the first peak and the energy of the third.

Figure 4.7: (Color online) The photoionization spectrum of the present work is compared with that of Grum-Grzhimailo et al. [24] for atomic hydrogen in a four-cycle laser pulse with a $\sin^2$ envelope applied to the electric field, having a peak intensity of $1 \times 10^{15} W/cm^2$ and a central frequency of $\omega = 0.3$ (152 nm).

Chapter 5

Results: the multiphoton regime

The past decade has witnessed the growth in the intensity, control, and characterization of few-cycle laser pulses. Control of the carrier envelope phase of infrared laser pulses, enables the engineering of the isolated attosecond pulse through the highly non-linear process of high harmonic generation. The pulse used in this paper is a mathematical idealization of the one crafted by Sansone et al. [53] and is shown inset in Fig. 5.1. This linearly-polarized, two-cycle, ultraviolet laser pulse has a central

Figure 5.1: (Color online) The linearly-polarized, two-cycle laser pulse [53] with a driving frequency of 36 eV and a peak field of $9.0 \times 10^9 V/cm$, which corresponds to an intensity of $1 \times 10^{15} W/cm^2$, and a carrier envelope phase of $\pi/2$.

photon energy of $\omega = 1.32$ (36 eV), peak intensity $I = 10^{15} W/cm^2$ i.e. $E_0 = 0.176$, and duration 9.62 (230.27 as). The power spectrum of the two cycle pulse (see Fig. 5.1) spans many bound and continuum states and can be thought of as a multimode laser with a continuum of frequencies.

In this section we present our best converged ionization and excitation results of the first three isoelectronic series subject to the attosecond laser pulse described in Fig. 5.1. Atomic hydrogen, He^+, Li^{2+} have a truncation thresholds of $\epsilon = 10^{-7}, 10^{-7}$, and 10^{-6} respectively; similarly, the cut parameters are $\xi = 0.05$, 0.059, and 0.03; and a simulation box $L = 3000$, 1000, and 1000, respectively. Access to the complete wave function allows us to calculate the energy, momentum, and angular spectra of the photoelectrons; along with the state resolved excitation probabilities and time evolution of dynamic variables: energy, dipole moment, and the inelastic transition probability.

5.1   Atomic hydrogen

The driving frequency of the laser pulse ($\omega = 1.32$) is much greater than the ionization potential of hydrogen. Thus single-photon ionization is expected to be the dominant. The ground state transition energies in atomic hydrogen are far below the peak of the laser's power spectrum confirm this (see Fig. 5.2c).

The typical dipole electron distribution is shown in both the double differential momentum in Fig. 5.2a and in the integrated angular cross section in Fig. 5.2b. A second peak near $k = 2$ corresponds to a two photon ionization. The arrow indicates the direction of the laser polarization. The relative strength of the ionization processes can be determined from the angular resolved ionization coefficients in Tab. 5.1 (see Section 5.2.1). The dipole transition to $\ell = 1$ is the leading term. The two and three photon processes diminish with a ratio consistent with perturbation theory.

Fig. 5.3 presents the evolution of various probabilities up to the end of the laser pulse. Ionization is the leading process (see Fig. 5.2c, Tab. 5.4). Single-photon
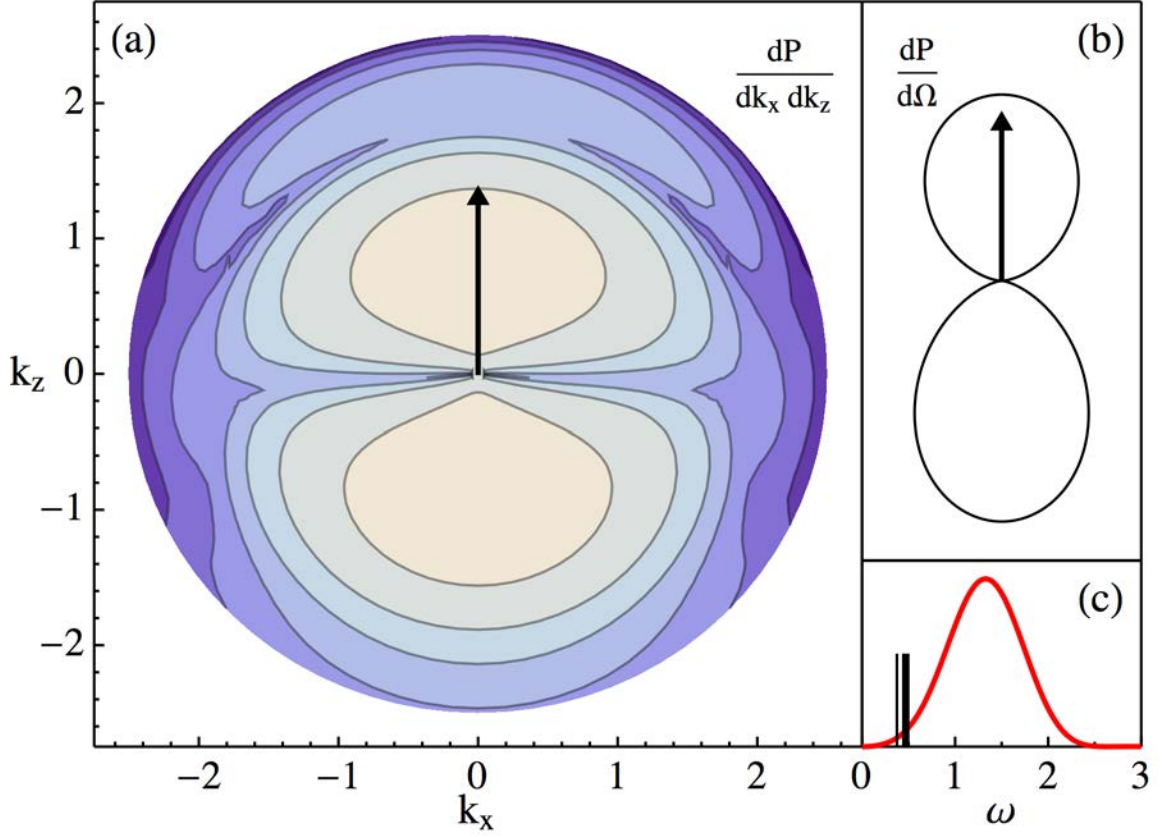
Figure 5.2: (Color online) (a) The full differential photoionization momentum distribution of atomic hydrogen and (b) angular distribution $dP/d\Omega$ from Eq. 3.32 are shown against the laser polarization access (the arrow). (c) Hydrogen's energy levels are superimposed on the laser's power spectrum.

ℓ	$|c_\ell^{ion}|^2$
0	3.22×10^{-4}
1	1.57×10^{-2}
2	1.75×10^{-4}
3	1.1×10^{-6}

Table 5.1: The angular resolved ionization coefficients of H, see Eq. (5.4).

Figure 5.3: (Color online) The total ionization probability, total inelastic excitation probability Eq. (4.3), and selected bound state probabilities $|\langle \psi_{n\ell 0} \mid \psi(t) \rangle|^2$ of H are plotted versus time. Due to azimuthal symmetry, m=0.

transitions to the bound p states are the next most probable event. The s state probabilities are more than 2 orders of magnitude smaller than those of the 2p states, and the d state transition probabilities are an order of magnitude smaller than those of the s state.

Fig. 5.4a shows the energy of hydrogen $\langle \mathscr{H} \rangle$, where $\mathscr{H}$ is the Hamiltonian from Eq. (2.21), oscillating with time as the loosely bound electron is driven across the atom by the laser field. The total inelastic excitation of hydrogen in Fig. 5.4c also oscillates with time. By contrast, He$^+$ (Fig. 5.4bc) shows no oscillatory behavior but periodically increases as the tightly bound electron is resonantly pumped into the 2p state.
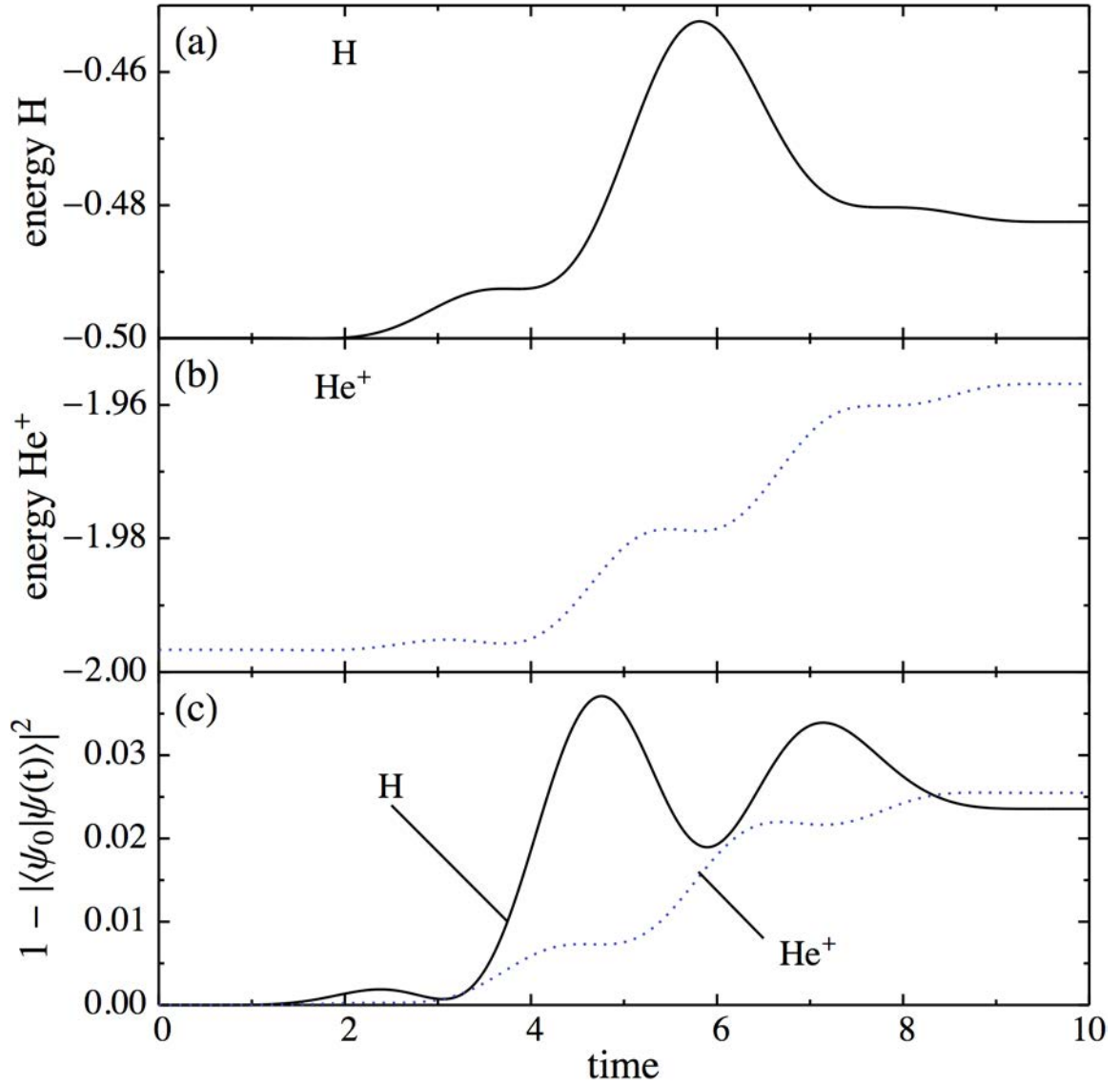
Figure 5.4: (Color online) The energy $\langle \mathcal{H} \rangle$ from Eq. (2.21) and total inelastic excitation from Eq. (4.3) for He^+ and H are shown as a function of time.

60

5.2 He$^+$

Fig. 5.5 presents the evolution of the ionization and excitation probabilities for He$^+$ during the laser pulse. The 2p excitation is the leading process followed by transition to the continuum, to 3p, 4p, and to other bound states. The two-photon transition probabilities to the s and d states are of mutually similar magnitude and are an order of magnitude smaller than ionization. The three-photon transitions to the f states are about three orders of magnitude below the transition to the s and d states.
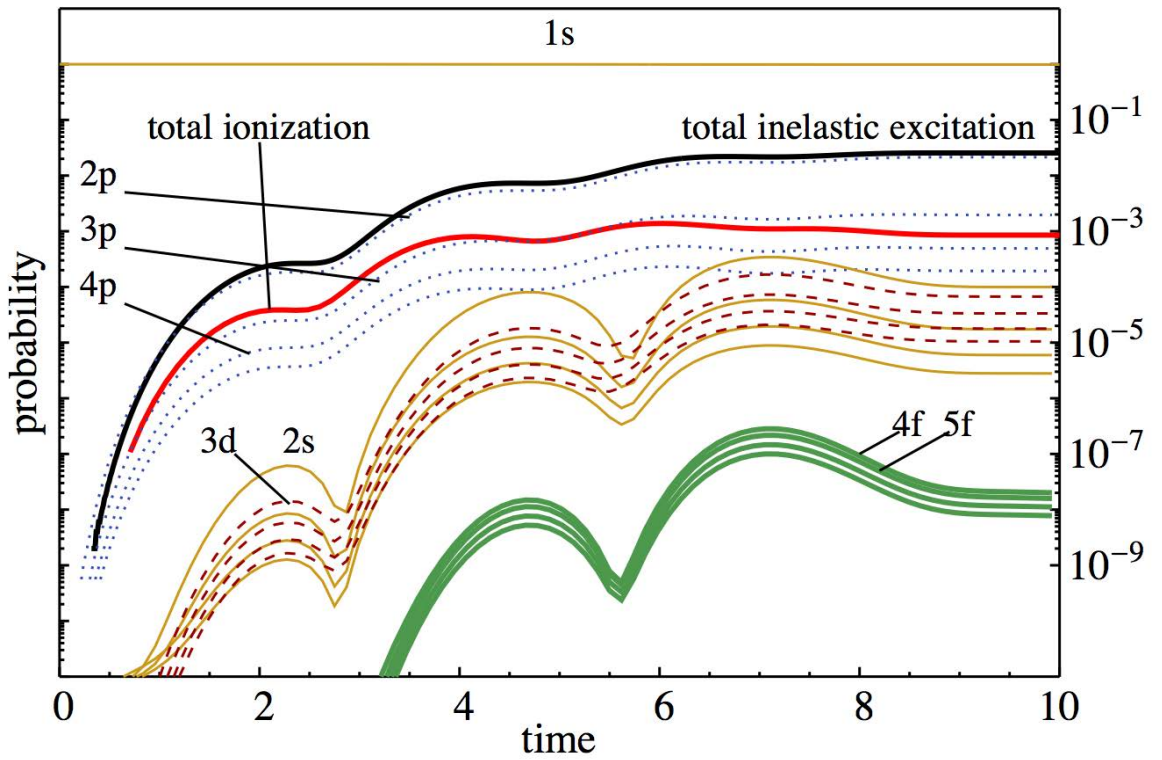
Figure 5.5: (Color online) The total ionization probability, total inelastic excitation probability Eq. (4.3), and selected bound state probabilities $|\langle \psi_{n\ell 0} \mid \psi(t) \rangle|^2$ of He$^+$ are plotted versus time. Due to azimuthal symmetry, m=0.

The horizontal arrows in Fig. 5.6c represent the competing ionization processes in He$^+$ from the bottom up: single-photon ionization, non-sequential 1s - $\mathbf{q}$ ionization, and sequential ionization 1s - 2p - $\mathbf{q}$. The leading single photon ionization channel is no longer dominant as it is with hydrogen. Table 5.2 shows the competition between

the p and d channels, as does the cancellation of their coherent superposition in Fig. 5.6a.
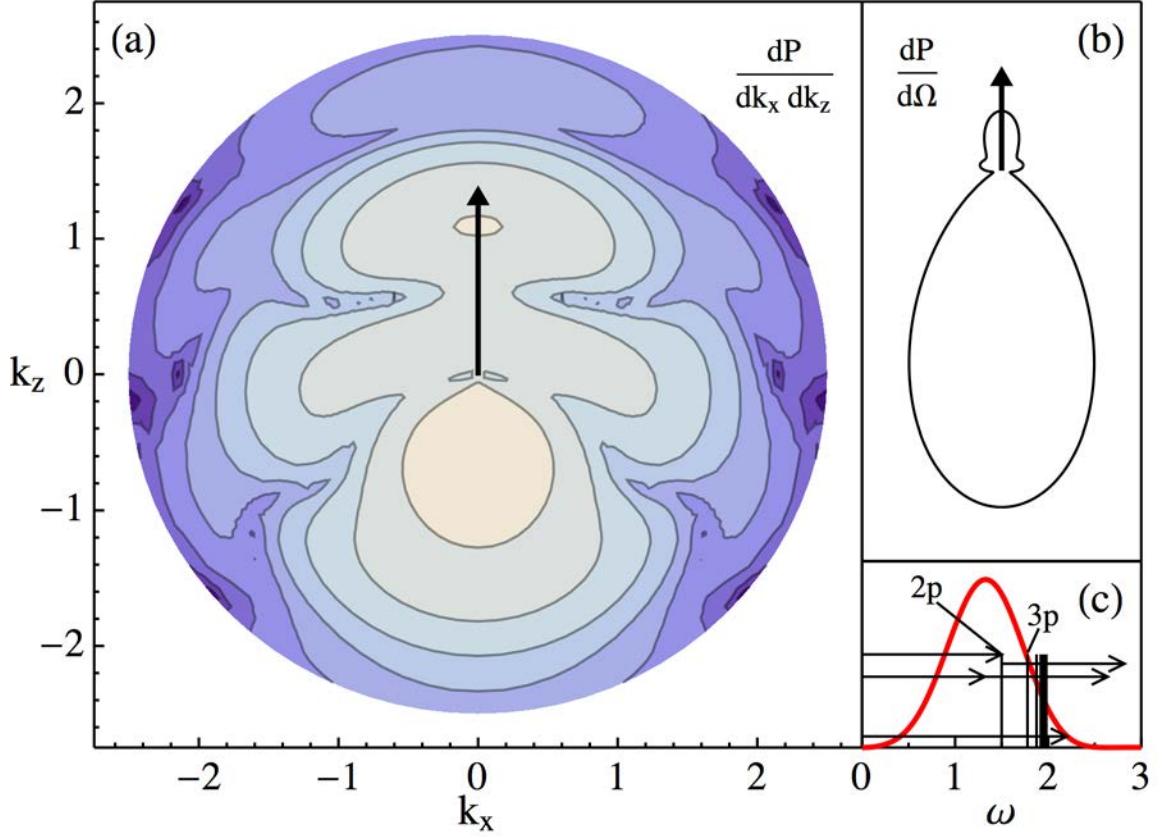
Figure 5.6: (Color online) (a) The fully differential photoionization momentum distribution of Li^{2+} and (b) angular distribution $dP/d\Omega$ from Eq. 3.32 are shown against the laser polarization access (the arrow). (c) The transition energies from the 2p (grayed) and the ground state are superimposed on the laser's power spectrum.

The distinctive $\ell = 2$ lobes projecting at right angles to the laser's polarization axis in the angular probability spectrum $dP/d\Omega$ (Fig. 5.6b) are the signature of two-photon ionization. The forward-backward ionization asymmetry of He^+ is not caused by an asymmetry in the laser pulse, as is the case when adjusting the carrier envelope phase but rather an interference between in the coherent sum in the multi-photon ionization channels. The weaker peak near $k = 2$ corresponds to a three photon ionization.

ℓ	$|c_\ell^{ion}|^2$
0	1.39×10^{-5}
1	5.20×10^{-4}
2	3.56×10^{-4}
3	3.88×10^{-6}

Table 5.2: The angular resolved ionization coefficients for He$^+$.

5.2.1 Angular ionization coeffcents

To determine the relative strength of each ionization process (see Table 5.2) we computed the difference between the total angular momentum resolved probability coefficients $|c_\ell|^2$ and those of the individual bound states. With the wave function ψ in the partial wave expansion

$$\psi(r,\theta) = \sum_\ell C_\ell(r)\, Y_{\ell 0}(\theta), \tag{5.1}$$

we obtain the ℓ'th radial distribution by projecting the wave function onto the ℓ'th spherical harmonic integrating over concentric spherical shells

$$C_\ell(r) = \langle Y_{\ell 0} \mid \psi \rangle_\Omega. \tag{5.2}$$

Since ψ is normalized, the total angular probability can be found by integrating $C_\ell(r)$.

$$|c_\ell|^2 = \int |C_\ell(r)|^2\, r^2 dr \tag{5.3}$$

The angular component of ionization is simply the difference between the total and bound probability of the ℓ'th component

$$|c_\ell^{ion}|^2 = |c_\ell|^2 - \sum_n |\langle \phi_{n\ell} \mid \psi \rangle|^2. \tag{5.4}$$

63

5.3 Li^{2+}

The ground 1s state of Li^{2+} lies 3.375 units of energy below the excitation to the 2p state and 4.5 units below the continuum edge which requires multiple photons from our laser pulse. The resulting transition probabilities are almost all below the numerical threshold ϵ; the metastable 2s state of Li^{2+} yields more interesting results.

Fig. 5.7 shows the dynamics of Li^{2+} initially in the 2s state where the ionization and dipole excitation to 3p are the leading events and nearly equal in probability. The $2s \to 1s$ channel has no allowed single-photon transitions, and the 1s probability does not follow the field as do the other states, but increases to a saturation point in the middle of the pulse. The $2s \to 2p$ transition is significantly smaller than the other p transitions since the power spectrum of the laser pulse is nearly 0 at the transition energy between the degenerate states (see inset). Its most probable 3 photon pathway is through the 4p followed by a transition to either the 3d or 3s before the final de-excitation.

Figure 5.7: (Color online) The total ionization probability, total inelastic excitation of Li^{2+} ($\xi = 0.1$) probability Eq. (4.3), and selected bound state probabilities $|\langle \psi_{n\ell 0} \mid \psi(t) \rangle|^2$ of H are plotted versus time. Due to azimuthal symmetry, m=0.

The three forward peaks in the photoionization spectrum of Li^{2+} in Fig. 5.8(a) at $q = 0.6$, 1.7, and 2.4 correspond to the single, double, and triple-photon ionization $k = \sqrt{2(n\,\omega - E_{2s})}$ at the driving frequency of $\omega = 1.32$. The weakest ionization potential in hydrogen had the least asymmetry while the largest ionization potential in He^+ corresponded to the greatest ionization asymmetry. Li^{2+} from the 2s state lies between these extremes both in the ionization potential and in the ionization asymmetry. This correlation may not be a coincidence.
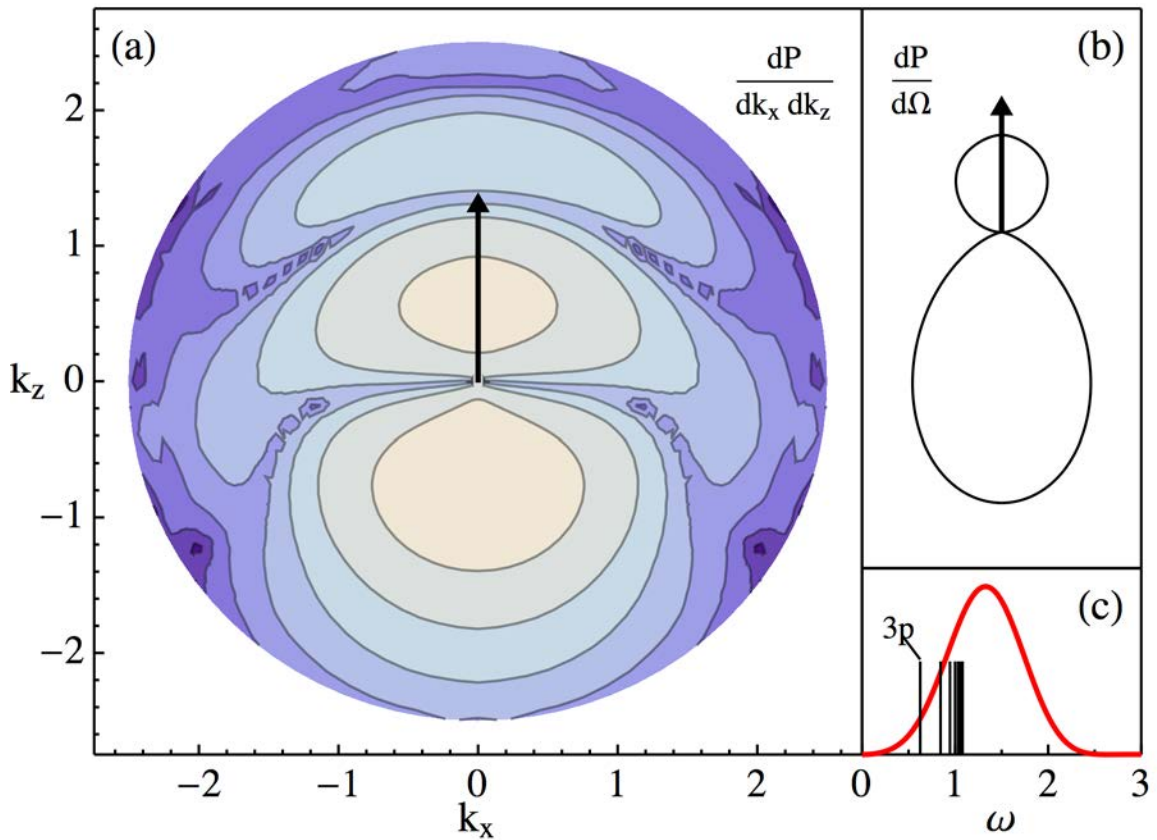
Figure 5.8: (Color online) (a) The fully differential photoionization momentum distribution of Li^{2+} and (b) angular distribution $dP/d\Omega$ from Eq. 3.32 are shown against the laser polarization access (the arrow). (c) The transition energies from the initial 2s state are superimposed on the laser's power spectrum.

ℓ	$\|c_\ell^{ion}\|^2$
0	6.14×10^{-5}
1	8.91×10^{-3}
2	4.19×10^{-4}
3	2.20×10^{-6}
4	5.25×10^{-8}

Table 5.3: The angular resolved ionization coefficients for Li^{2+}.

n	$\ell = 0$	1	2	3
1	0.97605			
2	2.09×10^{-5}	5.03×10^{-3}		
3	5.79×10^{-6}	1.27×10^{-3}	1.17×10^{-6}	
4	2.36×10^{-6}	5.08×10^{-4}	6.3×10^{-7}	2.6×10^{-11}
total	0.97609	7.56×10^{-3}	2.91×10^{-6}	2×10^{-10}

Table 5.4: The total bound and ionization probability of H are $P_{bound} = 0.984$ and $P_{ion} = 0.016$. $\varepsilon_{norm} = 5.6 \times 10^{-5}$.

n	$\ell = 0$	1	2	3
1	0.9745138			
2	9.96×10^{-5}	2.14×10^{-2}		
3	1.73×10^{-5}	1.96×10^{-3}	6.70×10^{-5}	
4	5.97×10^{-6}	4.92×10^{-4}	3.35×10^{-5}	2×10^{-8}
total	0.9746446	2.44×10^{-2}	1.55×10^{-4}	8.1×10^{-8}

Table 5.5: The total bound and ionization probability of He^+ are $P_{bound} = 0.999152$ and $P_{ion} = 8.49 \times 10^{-4}$. $\varepsilon_{norm} = 3.5 \times 10^{-6}$.

n	$\ell = 0$	1	2	3
1	2.81×10^{-6}			
2	0.965066	1.09×10^{-6}		
3	1.16×10^{-4}	1.27×10^{-2}	2.55×10^{-6}	
4	3.60×10^{-5}	5.02×10^{-3}	5.70×10^{-6}	1.2×10^{-8}
total	0.9652549	2.31×10^{-2}	3.10×10^{-5}	3.9×10^{-8}

Table 5.6: The total bound and ionization probability of Li^{2+} are $P_{bound} = 0.9884$ and $P_{ion} = 0.01035$. $\varepsilon_{norm} = 2.3 \times 10^{-3}$.

5.4 Conclusion

In the multiphoton regime the single and double photoionization of atomic hydrogen was presented. The energy and excitation dynamics of hydrogen and He^+ show the difference between resonant and non-resonant excitation. The competing sequential and non-sequential two-photon ionization in He^+ lead to a complex photoionization spectrum. The dynamics of the two-photon $2s \rightarrow 1s$ transition in $Li^{2+}(2s)$ was relatively independent of the field. The three-photon $2s \rightarrow 2p$ transition also showed peculiar behavior.

Chapter 6

Results: the tunneling regime

We turn to the computationally demanding tunneling regime where longer pulses have more time steps, the wave function fills a larger volume of space; and projection occurs on larger, finer continuum domains. We chose two-cycle, 800nm laser pulse with an intensity $I = 1 \times 10^{15} W/cm^2$ to allow comparison with the popular the titanium-sapphire experiments.

Figure 6.1: (Color online) A linearly-polarized, two-cycle laser pulse with a driving frequency of 1.5 eV and a carrier envelope phase of $-\pi/2$.

6.1 He$^+$

The laser pulse in Fig. 6.1 acting on He$^+$ yields a Keldysh parameter $\gamma = 0.68$ which is just inside the tunneling regime ($\gamma < 1$). The inelastic excitation probability in Fig. 6.2a ends at 2×10^{-5} which is just above the numerical threshold $\epsilon = 1 \times 10^{-5}$. The inelastic excitation is synchronized with the field, but the acceleration in Fig. 6.2b
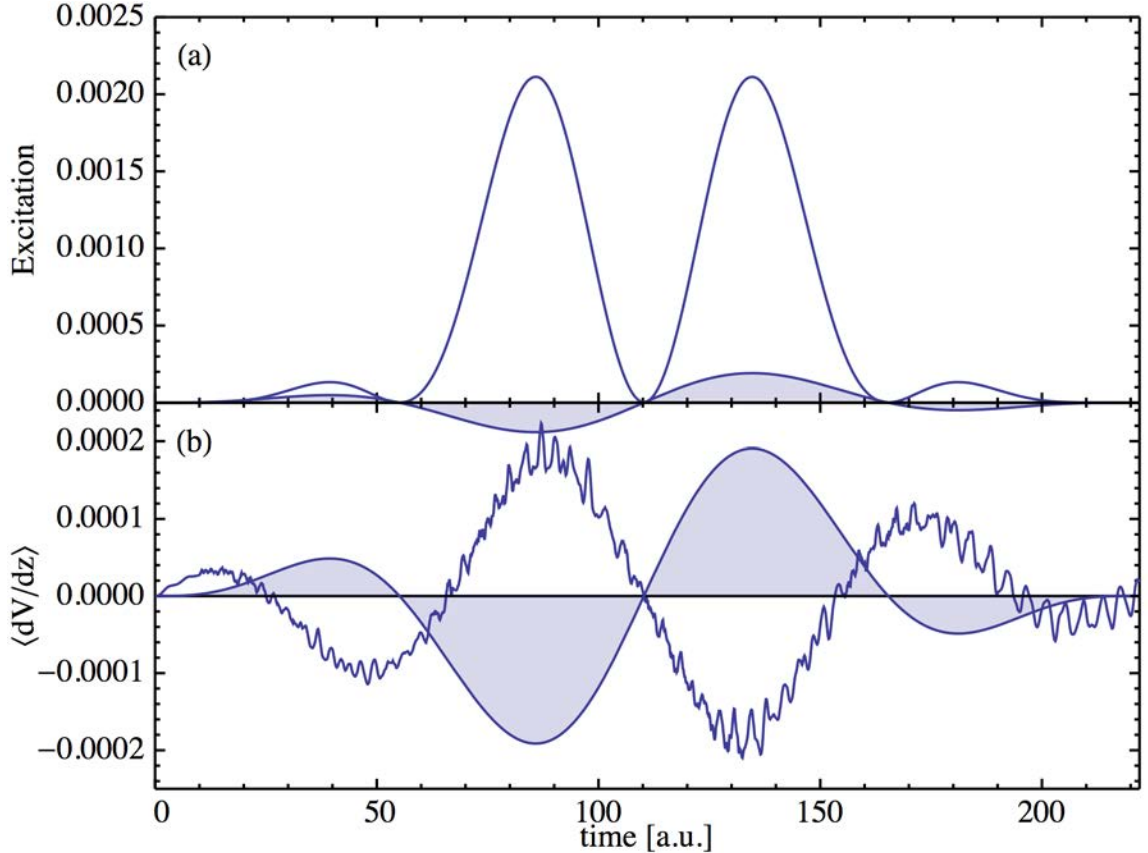
Figure 6.2: The dynamic variables of atomic hydrogen in a two-cycle 800nm laser pulse (a) energy (b) total inelastic excitation (c) the dipole $\langle z \rangle$ (d) the acceleration $\langle dV/dz \rangle$ more resolved levels.

is out phase. The rapid oscillations in Fig. 6.2b have a period which is just over 4 units of atomic time corresponding to the 1s - 2p transition energy of 1.5. The deeply bound electron must absorb 27 photons to make this transition and 36 photons for ionization. The ionization of He$^+$ in Fig. 6.3a is far below the numerical threshold,

and the peaks are not regularly spaced which is probably an artifact of the multimode laser pulse or the lack of numerical precision. The primary components of the angular distribution in Fig. 6.3b are aligned with the field. A surprisingly large secondary peak, is seen ejected azimuthally and smaller peaks seen between the two.

Figure 6.3: The photoionization spectrum of He$^+$ in a 800nm, two-cycle pulse with an intensity of $I = 1 \times 10^{15} W/cm^2$. The energy distribution (a) shows a series of peaks whose spacing is increasing with energy. The angular distribution in (b) shows two-fold symmetry axis.

6.2   Hydrogen

The laser pulse in Fig. 6.1 acting on atomic hydrogen yields a Keldysh parameter $\gamma = 0.34$ which is further into the tunneling regime than He6+. The electron gains huge quantities of energy as shown by the expectation value of the Hamiltonian in Fig. 6.4a. Fig. 6.4b shows less than 10% left in the ground state at the end of the pulse. This is the result of Over The Barrier Ionization (OTBI), which is described in Section 1.1.4.

Figure 6.4: The dynamic variables of atomic hydrogen in a two cycle 800nm laser pulse (a) energy (b) total inelastic excitation.

6.2.1 Above threshold ionization

The large number of photons needed for ionization give rise to non-linear phenomena in the ionization spectrum of hydrogen in Fig. 6.5. First, we notice a nearly unidirectional ionization in Fig. 6.5b which is due to OTBI. The photoionization energy spectrum in Fig. 6.5a has a rapidly decaying low-energy region that is reminiscent of perturbation regime (Eq. 1.11), and it forms a quasi-plateau around $E = 2$. ATI is characterized by peaks separated by integral multiples of the photon energy. Like He^+, the photoionization spectrum of hydrogen also exhibits uncharacteristic variable peak spacing that probably due to the broadband nature of the laser pulse.

The photoelectron spectrum computed by Grum-Grzhimailo et. al. [24] is used for comparison (see the lower panel in Fig. 6.5). We have the same intensity and wave length but they used a 10-cycle pulse. The magnitudes of both spectra are very close at the beginning and end of the pulse. They both have an envelope structure bounding the photoionization peaks. However, his pulse has a nearly constant decay
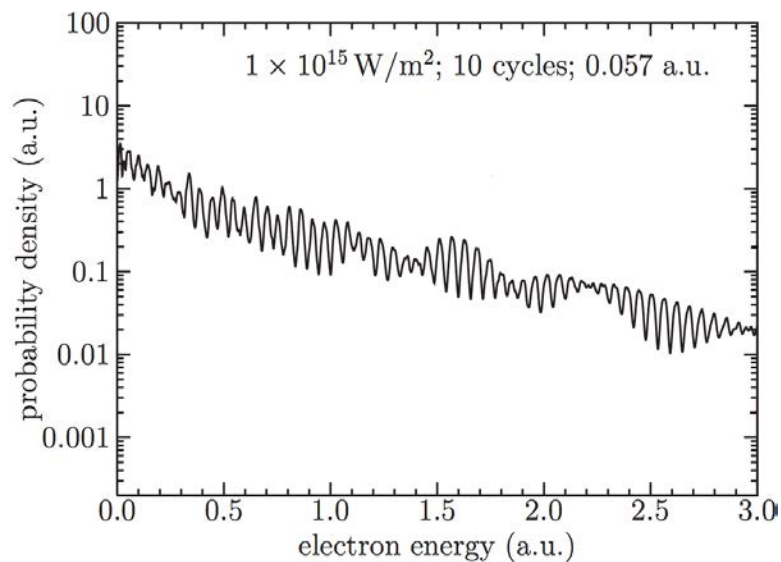
Figure 6.5: The photoionization spectrum of atomic hydrogen in a two-cycle pulse with intensity $I = 1 \times 10^{15} W/cm^2$. The energy distribution (a) shows a series of peaks whose spacing is increasing with energy. The angular distribution (b) shows the electron to be ionized in the negative direction. The lower panel is the photoionization spectrum of a 10-cycle pulse generated by Grum-Grzhimailo et. al. [24] shown for comparison. Note the different domains on the horizontal axis.

rate as E increases while ours varies. Over the reduced domain, Grum-Grzhimailo et al. has equally spaced energy peaks while our peak spacing is continually increasing. Convergence studies have not yet been performed in the tunneling domain, but I suspect that our variable peaks are an artifact of the broad-band laser pulse or the windowing effects of an insufficient L_{small}.

The classically allowed energies of an electron leaving a laser pulse have a maximum at $2.5U_p = 5.4 = 150eV$ (see Section 1.1.1). The rescattering mechanism has a cutoff at $10U_p = 21.4 = 584eV$. Our intensity ($I = 1 \times 10^{15}W/cm^2$) was well above the threshold for OTBI ($1.4 \times 10^{14}W/cm^2$), which has made it difficult to observe the rescattering cutoff at $10U_p$.

The structure of ATI can be seen without the obfuscating effects of OTBI. Even the inexpensive, low-accuraccy calculation ($L = 3000, \xi = 0.1, \epsilon = 10^{-3}$) reveals the characteristic peaks (Fig. 6.6) with a lower intensity ($I = 3 \times 10^{13}W/cm^2$). The predicted division between the direct ionization and rescattering regimes. The rapid

Figure 6.6: The (a) energy spectrum and (b) angular distribution of the photoionization of atomic hydrogen in a two-cycle pulse with intensity $I = 8 \times 10^{13}W/cm^2$.

decay in the direct ionization regime ends near $E = 0.8$, which is close to the predicted value at $2.5U_p = 0.88$. The plateau extends up $E = 2.4$ and the rescattering cutoff at $E = 3.3$ is near the predicted value at $10U_p = 3.5$.

6.2.2 Rescattering

Fig. 6.7 examines the angular distribution (AD) at select energies (from Fig. 6.6) in the low-intensity calculation. Panel (a) and (b) show the AD of two low energy peaks, and the complex AD in panel (c) comes from an energy between peaks. The finite resolution in the energy spectrum lead to some near-peak energies that include an extra lobe in the AD; panel (d) is one such value. The electron is ionized in the negative direction at energies below the $2.5U_p$ cutoff. The electron in panels (f)-(j) is ionization in the positive direction due to rescattering. The electron in panel (k) is primarily scattered down. A systematic study may reveal structure in the direction of the rescattered electron.

Figure 6.7: The angular distribution photoionization spectrum of atomic hydrogen in a two-cycle pulse with intensity $I = 8 \times 10^{13} W/cm^2$ at select energies.

6.2.3 High harmonic generation

We return to the intense ($I = 1 \times 10^{15} W cm^2$), two-cycle laser pulse. The dipole moment in Fig. 6.8a shows the electron traveling far from the atom. If the time evolution were continued the dipole would grow in the negative direction since OTBI has induced nearly complete ionization. This is confirmed by the acceleration (Fig 6.8b) at the end of the pulse which has returned to zero.
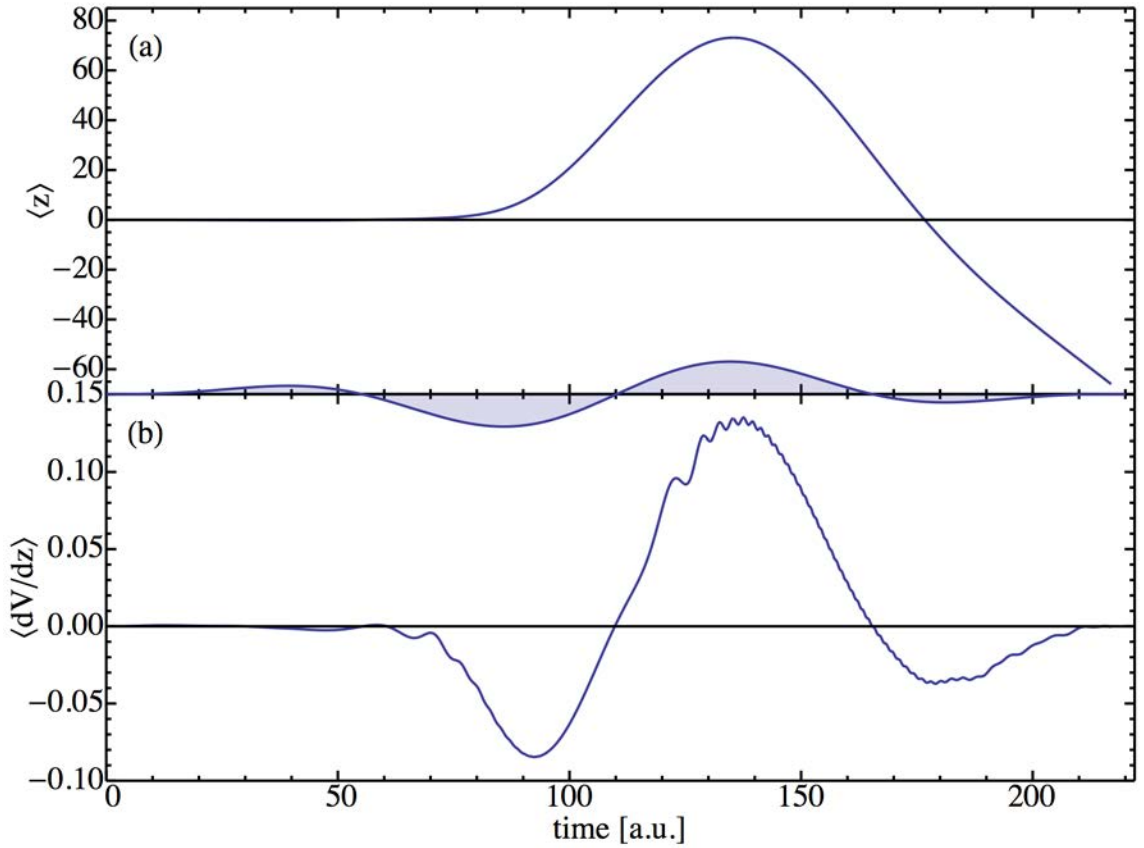
Figure 6.8: The dynamic variables of atomic hydrogen in a two cycle 800nm laser pulse (a) the dipole $\langle z \rangle$ (b) the acceleration $\langle dV/dz \rangle$

It is well known that accelerating charges produce radiation. The fine structure in Fig. 6.8b is evidence of radiative recombination as the high-energy electron wave

packet $c_k(t)$ recombines with the ground state.

$$P_k(t) = |\langle 1s \mid c_k(t) \, e^{ik \cdot r} \rangle|^2 \tag{6.1}$$

The HHG spectrum is generated by the square of the Fourier transform of the dipole acceleration;

$$P(\omega) = |\mathcal{F}[\langle \ddot{z} \rangle]|^2 \tag{6.2}$$

however, the numerical time derivative of the dipole moment introduces needless noise into the HHG spectrum. The interaction picture provides a more stable form with which to calculate the HHG spectrum.

$$P(\omega) = |\mathcal{F}[\langle \frac{dV}{dz} \rangle]|^2. \tag{6.3}$$

Eq. 6.3 gives a harmonic spectrum which includes the laser pulse. Since it is desirable to see which radiation components are generated from the atom, the electric field $\mathcal{E}(t)$ is removed from the acceleration before taking the Fourier transform.

$$P(\omega) = |\mathcal{F}[\mathcal{E}(t) - \langle \frac{dV}{dz} \rangle]|^2. \tag{6.4}$$

The HHG spectrum in Fig. 6.9 has an exponentially decaying region below $\omega = 0.3$. The plateau region extends to the edge of the graph. There are 18 peaks in Fig. 6.9 over the interval $\omega \in (1.0, 3.0)$ which correspond to an energy spacing of 0.056 which is within 2% off the photon energy.

6.3 Conclusion

A wide range of phenomena was shown in the tunneling regime. The field intensity, which ionized He$^+$ in the multiphoton regime (Ch. 5), left all but 0.002% in the ground state. The same pulse left hydrogen nearly completely ionized due to OTBI.

Figure 6.9: The HHG spectrum (Eq. 6.4) of atomic hydrogen under a two-cycle, 800nm laser pulse with an intensity of $I = 1 \times 10^{15} W/cm^2$. The laser corrected acceleration in the time domain is shown in the inset.

Reducing the intensity revealed above threshold ionization in hydrogen exposing the direct ionization and rescattering regimes in the angular and energy distributions. Finally, the OTBI of the intense pulse produced HHG in hydrogen.

Chapter 7

Results: molecular hydrogen

The computational flexibility of MADNESS's Cartesian coordinates is best exemplified in H_2^+. The mass of the internuclear coordinate (R) was scaled to accommodate a uniform application of the free particle propagator. The reduced mass of the two protons (μ) was used to scale the internuclear coordinate

$$s = \sqrt{\mu}R \qquad s \in [0, \sqrt{\mu}R_{max}] \qquad \mathbf{r} = (x, y, z, s) \tag{7.1}$$

Smoothing the nuclear potential (Section 3.4.1) and including the nuclear-nuclear potential V_{NN} was straightforward.

$$\hat{H} = -\frac{1}{2}\nabla^2 + V_{eN}(\mathbf{r}) + V_{NN}(s) + \mathbf{E}(t) \cdot \mathbf{r} \tag{7.2}$$

$$V_{eN}(\mathbf{r}) = V_\xi\left(\sqrt{(x - \frac{s}{2\sqrt{\mu}})^2 + y^2 + z^2}\right) + V_\xi\left(\sqrt{(x + \frac{s}{2\sqrt{\mu}})^2 + y^2 + z^2}\right)$$

$$V_{NN}(s) = \frac{\sqrt{\mu}}{s}$$

The initial internuclear wave function was approximated by the ground state harmonic oscillator

$$\psi(R) = \left(\frac{\mu\omega}{\pi}\right)^{\frac{1}{4}} e^{\mu\,\omega(R-R_0)^2/2} \qquad \psi(s) = \left(\frac{\omega}{\pi}\right)^{\frac{1}{4}} e^{\omega(s-\sqrt{\mu}R_0)^2/2} \tag{7.3}$$

centered at $R_0 = 2.0$ a.u.. The fully coupled 4D wave function was relaxed as described in Section 3.4.1.

It took just under an hour to run the 3D simulation of H_2^+ on the same computer and with the same parameters ($L = 300$, $k = 12$, and $\epsilon = 10^{-5}$) as atomic hydrogen mentioned in Section 4.1. The 4D H_2^+ ($L = 100$, $k = 8$, and $\epsilon = 10^{-4}$) took just under 5 hours running on a few thousand cores on the XT5 Cray at Oak Ridge National Laboratory. The time evolution of the 4D wave function was performed with the second order accurate Trotter propagator using the same separable, free-particle propagator G_0.

7.1 3D vs 4D

The electronic energy (expectation value of the Hamiltonian) is shown Fig. 7.1 as a function of time. At end of the pulse the energy of the 4D system increases slightly;
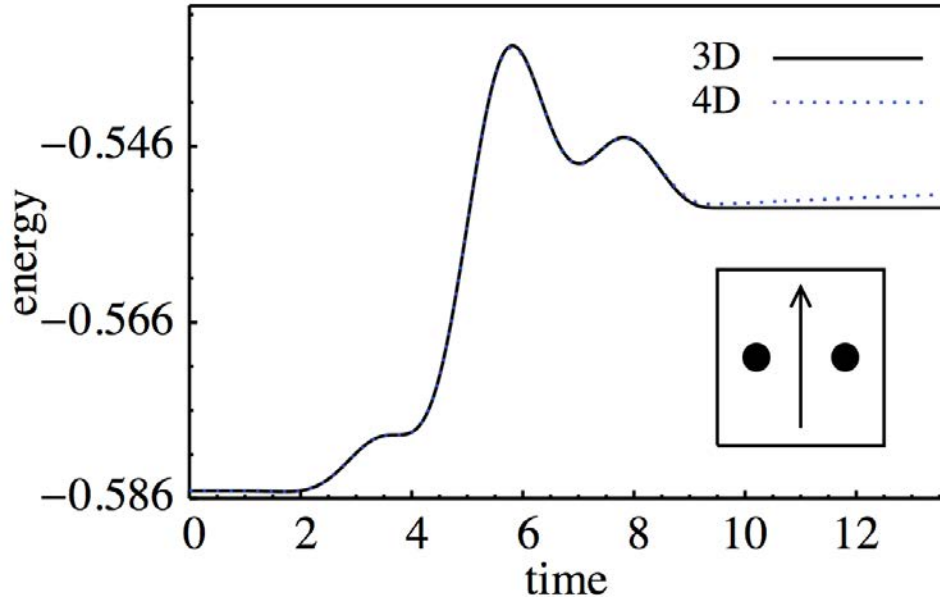
Figure 7.1: A comparison of the energy of the 3D and 4D simulations of H_2^+ oriented perpendicular to the laser field polarization axis, as shown by the inset.

this is probably time step error from the less-accurate Trotter propagation scheme. The agreement between the two simulations is expected, for on the attosecond time

scale, the nuclear motion is negligible. The application of an infrared pulse will trigger nuclear motion will highlight the breakdown of the fixed nuclear approximation.

7.2 Orientation

We next compare the behavior of the two orientations of the molecule. The energy dynamics have a striking difference originating from the different spatial ionization pathways. At a given distance from the center of a molecule, the potential energy along the molecule axis is the greatest making ionization less likely. Thus, the energy difference in the perpendicular orientation (Fig. 7.2) is less than that of the parallel orientation (Fig. 7.1).
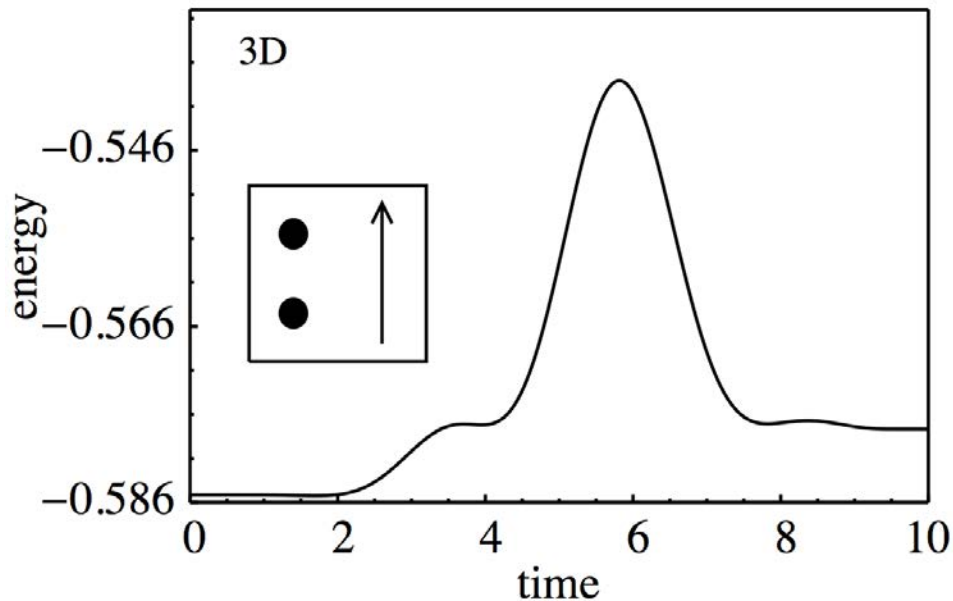
Figure 7.2: The energy H_2^+ whose internuclear axis is aligned parallel to the laser field polarization as shown by the inset.

The density of the electronic wave functions at the end of the pulse in Fig. 7.3 provides insight into ionization mechanisms. The perpendicular orientation in Fig. 7.3a shows the electron ionizing unobstructed. The ionization pathway of the electron in the aligned molecule (Fig. 7.3b) is blocked by the nuclei creating an interesting structure. A wave front extends in the forward direction and there are two

interesting lobes about 120 deg from the polarization axis. The holes in the electron
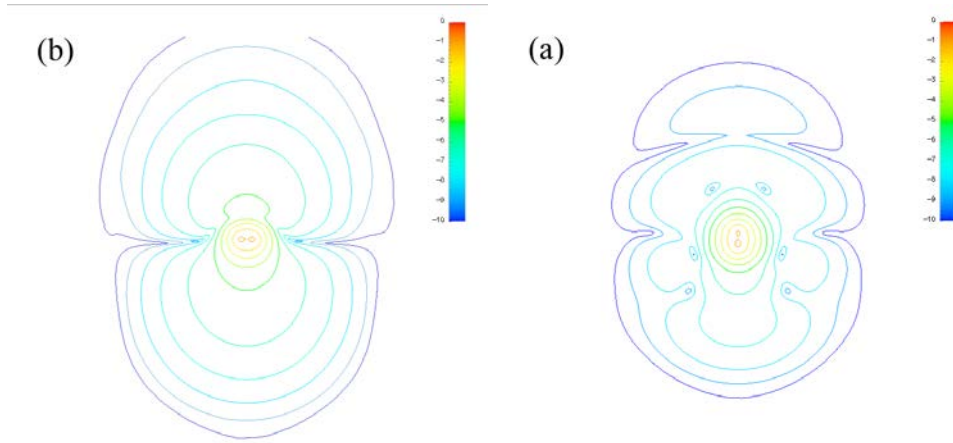
Figure 7.3: Isosurfaces of the probability density are shown at the end of the attosecond laser pulse for H_2^+ oriented (a) parallel and (b) perpendicular to the field polarization.

wave function look strangely similar to the vortices presented by Ovchinnikov et al. [44]. Since they are not present in the perpendicular orientation of the molecule, they may be destructive interference pockets from multiple scattering in the centers in parallel aligned molecule.

Continued time evolution of the wave function reveals strikingly different behavior in the dynamic acceleration of the electron (see Fig. 7.4). The oscillating acceleration of the parallel oriented molecule has an expanding envelope that signifies two excited states are present in the wave function. The constant amplitude oscillation of the acceleration of the perpendicular orientation signifies a single excited state. Ironically, there are no bound excited states in H_2^+ when the internuclear distance is allowed to vary. The 3D simulation with a fixed internuclear distance does have excited states, but shares the Rydberg spectrum of He^+.

When comparing the acceleration during the field, the perpendicular orientation oscillates faster and with larger amplitude due to the ease of oscillation during the pulse. Conversely, the parallel orientation doesn't accelerate as vigorously and there

is a "drag" slightly slowing the period of oscillation, which can be seen at the end of the pulse.
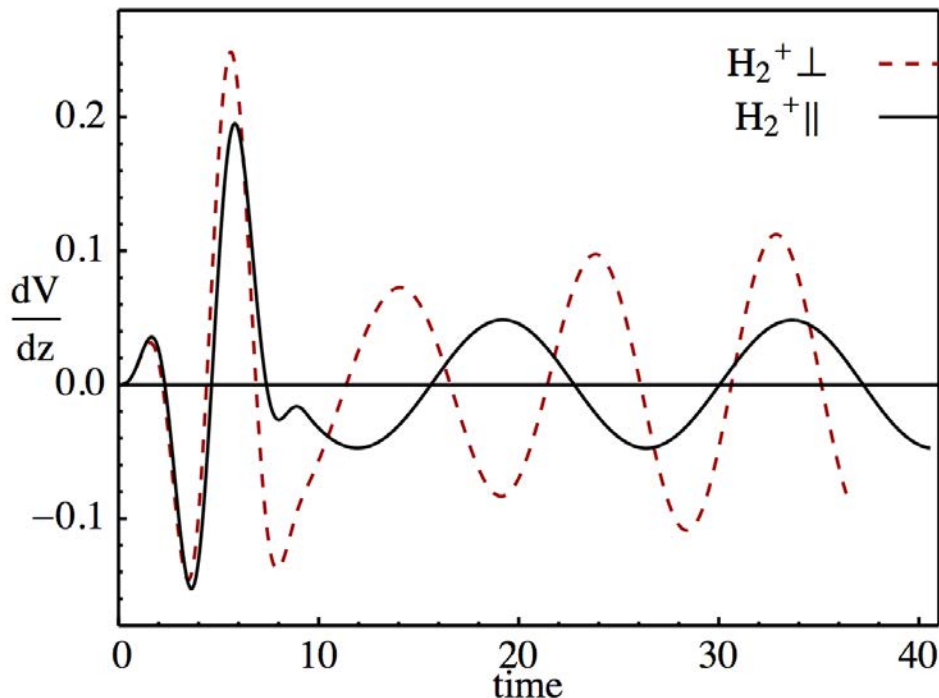
Figure 7.4: The acceleration in the z direction vs time. The purple curve is the perpendicular orientation and the red curve is the parallel orientation

7.3 Conclusion

The extension of our scheme to higher dimensions was demonstrated by including the internuclear separation of molecular hydrogen as a dynamic variable on equal footing with the electron. Agreement between the 3D and 4D simulation in the high frequency domain was encouraging, but not spectacular. Different dynamic behavior was observed for the parallel and perpendicular orientations of the intermolecular axis to the laser polarization axis. Future calculations with lower frequency light are expected to show the breakdown of the fixed nuclear approximation.

Chapter 8

Conclusions

Atomic, molecular, and optical physics has been driven by advances in laser technology over the last few decades. Shorter pulses, more intense fields, and better control of the sub-cycle dynamics have expanded the horizons of both experiment and theory. Our scheme for solving the time dependent Schrödinger equation (TDSE) adds to the growing body of computational methods which seek to explain these new domains.

A convergence study was presented in the multiphoton regime for hydrogenic systems subject to an attosecond laser pulse for the following numerical parameters: box size, numerical threshold, time step, and cut.

The attosecond laser pulse lead to the following observations: a comparison of the energy and excitation dynamics of hydrogen and He^+ contrasted resonant and non-resonant excitation, the competing sequential and non-sequential two-photon ionization in He^+ led to a complex photoionization spectrum, the dynamics of the two-photon $2s \rightarrow 1s$ transition in $Li^{2+}(2s)$ and the three-photon $2s \rightarrow 2p$ were qualitatively different to the rest of the transitions.

The 800nm pulse uncovered a wide range of phenomena. The field intensity, which ionized He^+ in the multiphoton regime, left all but 0.002% in the ground state. This same pulse induced over the barrier ionization in hydrogen leaving only few percent

bound. Reducing the intensity in hydrogen revealed above threshold ionization by exposing direct ionization and rescattering in the angular and energy distributions. Finally, the intense pulse produced an oscillating acceleration which is characteristic of high harmonic generation.

The extension of our scheme to higher dimensions was demonstrated in molecular hydrogen by the inclusion of an internuclear separation in the wave function on equal footing with the 3D electron coordinates. The energies of simulations with fixed and variable internuclear separation agreed in the attosecond regime. A general purpose MCSCF scheme in MADNESS will offer unique benefits in facilitating the choice of single particle reference states.

Bibliography

[1] P Agostini and LF DiMauro. The physics of attosecond light pulses. *Reports On Progress In Physics*, 67(6):813–855, 2004. vii, 10

[2] P Agostini, F Fabre, G MAINFRAY, G Petite, and N Rahman. Free-Free Transitions Following Six-Photon Ionization of Xenon Atoms. *Physical Review Letters*, 42(17):1127–1130, April 1979. 5

[3] B Alpert, G Beylkin, D Gines, and L Vozovoi. Adaptive solution of partial differential equations in multiwavelet bases. *Journal of Computational Physics*, 182(1):149–190, 2002. 29, 32, 38

[4] S Augst, D Strickland, D Meyerhofer, S Chin, and J Eberly. Tunneling ionization of noble gases in a high-intensity laser field. *Physical Review Letters*, 63(20):2212–2215, November 1989. 6, 7

[5] T Auguste, P Monot, L Lompre, G MAINFRAY, and C MANUS. Multiply charged ions produced in noble gases by a 1 ps laser pulse at lambda =1053 nm. *Journal Of Physics B-Atomic Molecular And Optical Physics*, 25:4181, October 1992. 6

[6] A Becker and F Faisal. Intense-field many-body S-matrix theory. *Journal Of Physics B-Atomic Molecular And Optical Physics*, 38(3):R1–R56, 2005. 14, 17

[7] W. Becker, F. Grasbon, R. Kopold, D.B. Miloevi, G.G. Paulus, and H. Walther. Above-threshold ionization: From classical features to quantum effects.

volume 48 of *Advances In Atomic, Molecular, and Optical Physics*, pages 35 – 98. Academic Press, 2002. 14

[8] Hans Bethe and Edwin Salpeter. *Quantum Mechanics of One- and Two-Electron Atoms*. Plenum, 1957. 6, 13

[9] B H Bransden and C J Joachain. *Physics of Atoms and Molecules*. Prentice Hall, 2003. 22

[10] P G Burke, C J Noble, and V M Burke. *Advances In Atomic, Molecular, and Optical Physics*, volume 54 of *Advances In Atomic, Molecular, and Optical Physics1049250X*. Elsevier, 2006. 16

[11] SA Chin and CR Chen. Fourth order gradient symplectic integrator methods for solving the time-dependent Schrödinger equation. *The Journal of Chemical Physics*, 114:7338, 2001. 36, 49

[12] SI Chu and J Cooper. Threshold shift and above-threshold multiphoton ionization of atomic-hydrogen in intense laser fields. *Physical Review A*, 32(5):2769–2775, 1985. 1

[13] P B Corkum and Ferenc Krausz. Attosecond science. *Nature Physics*, 3(6):381–387, 2007. vii, 9

[14] P Eckle, A N Pfeiffer, C Cirelli, A Staudte, R Dorner, H G Muller, M Buttiker, and U Keller. Attosecond Ionization and Tunneling Delay Time Measurements in Helium. *Science*, 322(5907):1525–1529, December 2008. 1

[15] F H M Faisal. *Theory of Multiphoton Proccesses*. Plenum, 1987. 14

[16] G Fann, G Beylkin, RJ Harrison, and KE Jordan. Singular operators in multiwavelet bases. *IBM Journal Of Research And Development*, 48(2):161–171, 2004. 29

[17] J Feist, S Nagele, R Pazourek, E Persson, B I Schneider, L A Collins, and J Burgdoerfer. Nonsequential two-photon double ionization of helium. *Physical Review A*, 77(4):043420, 2008. 17

[18] J Feist, S Nagele, C Ticknor, B Schneider, L Collins, and J Burgdörfer. Attosecond Two-Photon Interferometry for Doubly Excited States of Helium. *Physical Review Letters*, 107(9), August 2011. 12

[19] Mihai Gavrila. *Atoms in Intense Laser Fields*. Academic Press, 1992. 3

[20] Paul Gibbon. *Short Pulse Laser Interactions with Matter*. Imperial College Press, 2005. 3

[21] Ariel Gordon, Robin Santra, and Franz X Kärtner. Role of the Coulomb singularity in high-order harmonic generation. *Physical Review A*, 72(6):063411, December 2005. 40

[22] Eleftherios Goulielmakis, Zhi-Heng Loh, Adrian Wirth, Robin Santra, Nina Rohringer, Vladislav S Yakovlev, Sergey Zherebtsov, Thomas Pfeifer, Abdallah M Azzeer, Matthias F Kling, Stephen R Leone, and Ferenc Krausz. Real-time observation of valence electron motion. *Nature*, 466(7307):739–743, August 2010. 1

[23] G F Gribakin and M Yu Kuchiev. Multiphoton detachment of electrons from negative ions. *Physical Review A*, 55(5):3760–3771, May 1997. 16

[24] Alexei N Grum-Grzhimailo, Brant Abeln, Klaus Bartschat, Daniel Weflen, and Timothy Urness. Ionization of atomic hydrogen in strong infrared laser fields. *Physical Review A*, 81(4):043408, apr 2010. ix, xi, 55, 71, 72

[25] RJ Harrison, GI Fann, T Yanai, Z Gan, and G Beylkin. Multiresolution quantum chemistry: Basic theory and initial applications. *The Journal of Chemical Physics*, 121(23):11587–11598, 2004. 29, 35, 40, 51

[26] Robert Harrison. Implementation notes. http://code.google.com/p/m-a-d-n-e-s-s/downloads/list, November 2011. 29, 39

[27] S X Hu and L A Collins. Attosecond Pump Probe: Exploring Ultrafast Electron Motion inside an Atom. *Physical Review Letters*, 96(7), February 2006. 1

[28] J Itatani, J Levesque, D Zeidler, Hiromichi Niikura, H Pépin, J-C Kieffer, P B Corkum, and D M Villeneuve. Tomographic imaging of molecular orbitals. *Nature*, 432(7019):867–871, December 2004. 1

[29] Y H Jiang, A Rudenko, J F Perez-Torres, O Herrwerth, L Foucar, M Kurka, K U Kühnel, M Toppin, E Plésiat, F Morales, F Martín, M Lezius, M F Kling, T Jahnke, R Dorner, J L Sanz-Vicario, J van Tilborg, A Belkacem, M Schulz, K Ueda, T J M Zouros, S Düsterer, R Treusch, C D Schröter, R Moshammer, and J Ullrich. Investigating two-photon double ionization of D_2 by XUV-pump–XUV-probe experiments. *Physical Review A*, 81(5):051402(R), May 2010. 1

[30] L V Keldysh. Ionization in field of a strong electromagnetic wave. *Soviet Physics JETP-USSR*, 20(5):1307, 1965. 4

[31] Jeffrey L Krause, Kenneth J Schafer, and Kenneth C Kulander. High-order harmonic generation from atoms and ions in the high intensity regime. *Physical Review Letters*, 68(24):3535–3538, June 1992. 10

[32] Ferenc Krausz and Misha Ivanov. Attosecond physics. *Reviews Of Modern Physics*, 81(1):163–234, 2009. vii, 10, 11, 12

[33] U Lambrecht, L Dimou, and FHM FAISAL. Ab initio rates of multiphoton ionization of the isoelectronic species H, He+, and Li2+ in the vuv and xuv frequency regions. *Physical Review A*, 57(4):2832–2840, 1998. 16

[34] L D Landau and E M Lifshitz. *Quantum Mechanics*. Butterworth Heinemann, 1958. 41

[35] M Lewenstein, Ph Balcou, M Yu Ivanov, Anne L'huillier, and P B Corkum. Theory of high-harmonic generation by low-frequency laser fields. *Physical Review A*, 49(3):2117–2132, March 1994. 10

[36] L Lompre. Multiphoton ionisation of He atoms at 532 nm. *Physics Letters A*, 112(6-7):319–322, November 1985. vi, 5

[37] M A Lysaght, H W Van Der Hart, and P G Burke. Time-dependent R -matrix theory for ultrafast atomic processes. *Physical Review A*, 79(5):1–11, May 2009. 16

[38] Alexei Markevitch, Stanley Smith, Dmitri Romanov, H Bernhard Schlegel, Misha Ivanov, and Robert Levis. Nonadiabatic dynamics of polyatomic molecules and ions in strong laser fields. *Physical Review A*, 68(1), July 2003. 14

[39] J Mauritsson, T Remetter, M Swoboda, K Kluender, A L'Huillier, K J Schafer, O Ghafur, F Kelkensberg, W Siu, P Johnsson, M J J Vrakking, I Znakovskaya, T Uphues, S Zherebtsov, M F Kling, F Lepine, E Benedetti, F Ferrari, G Sansone, and M Nisoli. Attosecond Electron Spectroscopy Using a Novel Interferometric Pump-Probe Technique. *Physical Review Letters*, 105(5):053001, 2010. 1

[40] A McPherson, G Gibson, H Jara, U Johann, T S Luk, A McIntyre, K Boyer, and C K Rhodes. Studies of Multiphoton Production of Vacuum Ultraviolet-Radiation in the Rare-Gases. *Journal Of The Optical Society Of America B-Optical Physics*, 4(4):595–601, 1987. 9

[41] Marvin Mittleman. *Introduction to the Theory of Laser-Atom Interactions*. Plenum, 1993. 22

[42] K W Morton and D F Mayers. *Numerical Solution of Partial Differential Equations*. Cambridge, 2005. 38

[43] N Naumova, I Sokolov, J Nees, A Maksimchuk, V Yanovsky, and G Mourou. Attosecond electron bunches. *Physical Review Letters*, 93(19):195003, 2004. 14

[44] S Ovchinnikov, J Sternberg, J Macek, Teck-Ghee Lee, and D Schultz. Creating and Manipulating Vortices in Atomic Wave Functions with Short Electric Field Pulses. *Physical Review Letters*, 105(20), November 2010. 1, 81

[45] Rüdiger Paschotta. *Encyclopedia of Laser Physics and Technology*. Wiley-VCH, 2008. 3

[46] G Paulus, F Zacher, H Walther, A Lohr, W Becker, and M Kleber. Above-Threshold Ionization by an Elliptically Polarized Field: Quantum Tunneling Interferences and Classical Dodging. *Physical Review Letters*, 80(3):484–487, January 1998. 16

[47] G Petite and P Agostini. Intensity dependence of non-perturbative above-threshold ionisation spectra: experimental study. *Journal of Physics B: Atomic*, 1988. vi, 5, 7

[48] G Petite, F Fabre, P Agostini, M Crance, and M Aymar. Nonresonant multiphoton ionization of cesium in strong fields: Angular distributions and above-threshold ionization. *Physical Review A*, 29(5):2677–2689, May 1984. 14

[49] M S Pindzola and F Robicheaux. Time-dependent close-coupling calculations of correlated photoionization processes in helium. *Physical Review A*, 57(1):318–324, January 1998. 1

[50] M S Pindzola, F Robicheaux, S D Loch, J C Berengut, T Topcu, J Colgan, M Foster, D C Griffin, C P Ballance, D R Schultz, T Minami, N R Badnell, M C Witthoeft, D R Plante, D M Mitnik, J A Ludlow, and U Kleiman. The time-dependent close-coupling method for atomic and molecular collision processes. *Journal Of Physics B-Atomic Molecular And Optical Physics*, 40(7):R39–R60, March 2007. 17

[51] Tenio Popmintchev, Ming-Chang Chen, Paul Arpin, Margaret M Murnane, and Henry C Kapteyn. The attosecond nonlinear optics of bright coherent X-ray generation. *Nature Photonics*, 4(12):822–832, December 2010. 12

[52] E A Pronin, Anthony F Starace, M V Frolov, and N L Manakov. Perturbation theory analysis of attosecond photoionization. *Physical Review A*, 80(6):063403, 2009. 14, 55

[53] G Sansone, E Benedetti, F Calegari, C Vozzi, L Avaldi, R Flammini, L Poletto, P Villoresi, C Altucci, R Velotta, S Stagira, S De Silvestri, and M Nisoli. Isolated single-cycle attosecond pulses. *Science*, 314(5798):443–446, 2006. ix, 56

[54] W F Schneider. Electron correlation. http://www.nd.edu/~wschnei1/courses/CBE_547/Lectures/Lecture6/Lecture6.pdf, October 2009. 19

[55] Armin Scrinzi, Michael Geissler, and Thomas Brabec. Ionization Above the Coulomb Barrier. *Physical Review Letters*, 83(4):706–709, July 1999. 14

[56] B Shore and P Knight. Enhancement of high optical harmonics by excess-photon ionisation. *Journal of Physics B: Atomic and Molecular Physics*, 20:413, January 1987. 9

[57] David J. Tannor. *Introduction to Quantum Mechanics: A time-dependent perspective.* University Science Books, 2007. 37

[58] M Uiberacker, Th Uphues, M Schultze, A J Verhoef, V Yakovlev, M F Kling, J Rauschenberger, N M Kabachnik, H Schroeder, M Lezius, K L Kompa, H G Muller, M J J Vrakking, S Hendel, U Kleineberg, U Heinzmann, M Drescher, and F Krausz. Attosecond real-time observation of electron tunnelling in atoms. *Nature*, 446(7136):627–632, 2007. 1

[59] Nicholas Vence, Robert Harrison, and Predrag Krstić. Attosecond electron dynamics: a multiresolution approach. *Physical Review A*, to be published, 2012. 2

[60] T Yanai, GI Fann, ZT Gan, RJ Harrison, and G Beylkin. Multiresolution quantum chemistry in multiwavelet bases: Analytic derivatives for Hartree-Fock and density functional theory. *The Journal of Chemical Physics*, 121(7):2866–2876, 2004. 29

Vita

Summary

Nicholas Vence was born on May 15, 1980 in Colombia, South Carolina. He is a computational, atomic physicist looking to explore his interest in ultrafast, atomic physics research as a post-doc. His research collaboration developed an ab initio solution to the time dependent Schrdinger equation, and he is intent on joining a research community which enjoys a cross-pollination between theory and experiment. Dr. Vence enjoys communication and is eager to continue mentoring, publishing, and speaking as he extends his understanding of computation and attosecond science.

Education

- 2004 - 2011   University of Tennessee at Knoxville, PhD in Computational Physics completed November 2011 Advisors: Robert Harrison & Predrag Krstić Thesis title: *Laser-atom interactions: a multiresolution approach*

- 1998 - 2004   Southern Adventist University, BS Physics, BA Math Senior Project: 2D space-time diagrams Math Club: VP & President

Skills & Tools

- C++: STL, templates, external libraries, autotools

- Bash & Python scripting

- Mathematica programming & visualization

- Publishing tools: LaTeX, html[1], Wikipedia[2], stackoverflow[3]

- Part of the MADNESS [4] development team

- UNIX tools: vim/emacs, regex, subversion ...

- Parallel programming

- Familiarity with: Boost, OpenMP, MPI, Fortran

Work Experience

- 2004 - 2011   Teaching & Graduate Assistant   University of Tennessee

- 1999 - 2004   Physics Tutor & Lab Assistant   Southern Adventist University

- 2000 - 2001   High school math and physics teacher   Yap, Micronesia

- 1997 - 2005   Counselor, Rock Climbing & Assistant Director   Camp Alamisco

Presentations & Publications

- Southeast Theoretical Chemistry Association 2008, Laser-atom interactions (poster), Tuscaloosa AL

- March American Physical Society Meeting 2009, Single electron systems in a short strong laser pulse (contributed talk), Pittsburgh PA

- International Conference in Photonic Electronic and Atomic Collisions 2009, Hydrogenic ions in an attosecond laser pulse (poster), Kalamazoo MI

- March American Physical Society Meeting 2010, Multiresolution treatment of hydrogenic ions in a strong laser (poster), Portland OR

- Division of Atomic Molecular and Optical Physics 2010, Hydrogenic systems in a strong laser (poster), Houston TX

- Conference of Computational Physics 2011, Hydrogenic atoms in a strong few-cycle laser pulse (contributed talk), Gatlinburg TN

- Physical Review A 2011, Attosecond electron dynamics: a multiresolution approach (submitted paper)

Links

[1] http://web.utk.edu/~nevence/index.html

[2] http://en.wikipedia.org/wiki/Configure_script

[3] http://stackoverflow.com/questions/7039189/which-openmp-pragma-do-i-use-for-a-blocking-for-loop

[4] http://code.google.com/p/m-a-d-n-e-s-s/